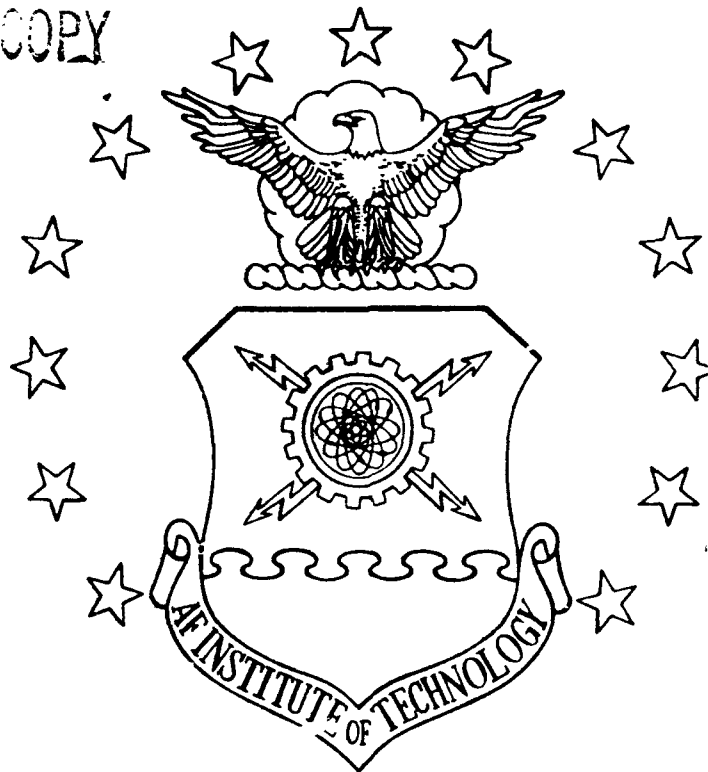


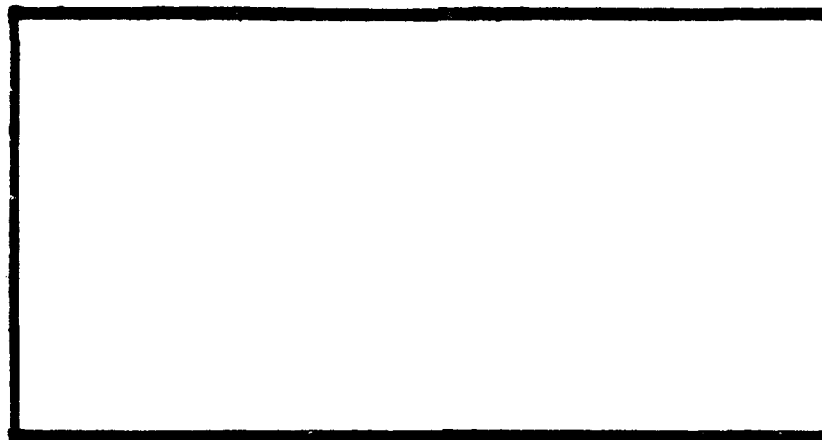
AD-A230 584

DTIC FILE COPY

1

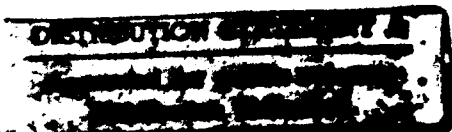


DTIC
ELECTE
JAN 07 1991
S B D



DEPARTMENT OF THE AIR FORCE
AIR UNIVERSITY
AIR FORCE INSTITUTE OF TECHNOLOGY

Wright-Patterson Air Force Base, Ohio



91 1 3 129

AFIT/GEO/ENG/90D-09

①

OPTICAL
IMAGE SEGMENTATION
USING
WAVELET FILTERING
TECHNIQUES

THESIS

Christopher P. Veronin
Captain, USAF

AFIT/GEO/ENG/90D-09

DTIC
ELECTE
JAN 07 1991
S B D

Approved for public release; distribution unlimited

AFIT/GEO/ENG/90D-09

OPTICAL
IMAGE SEGMENTATION
USING
WAVELET FILTERING
TECHNIQUES

THESIS

Presented to the Faculty of the School of Engineering
of the Air Force Institute of Technology
Air University
In Partial Fulfillment of the
Requirements for the Degree of
Master of Science in Electrical Engineering

Christopher P. Veronin, B.S.E.E.
Captain, USAF

December 1990

Approved for public release; distribution unlimited

Preface

First of all, I'd like to state that I thoroughly enjoyed this thesis project: being able to directly apply the Fourier Optic concepts learned in the classroom and the lab; working hands-on with lasers, optics, cameras, holographic plates, digital framegrabbers, and LCTVs; and creatively designing the optical setup, the spatial filters, and the presentation of the results. For these reasons, I highly recommend undertaking an optical experimental thesis to anyone wishing this kind of advice.

I'd like to thank my thesis committee members, Dr. Matthew Kabrisky and Dr. Byron Welsh for their time, insights, and suggestions concerning this thesis project. I'd especially like to thank my thesis advisor, Dr. Steve Rogers, for teaching me all that I know about Fourier Optics, giving me room to be creative, and being there with advice when I was butting my head up against a wall (down Larry). I'd also like to thank my predecessor and sponsor, Captain Kevin Ayer, WRDC/AARI-2, for his support and continued interest in this topic and for trusting me with those two, pilferable Sony Video Walkman LCTVs. Additional thanks should go to Osvaldo Perez, ASD/ENAML, for loaning me the quad input video system, letting me dub the real-time FLIR imagery, and showing me the ropes on LCTVs and precise optical bench alignment, and Captain Kevin Priddy for helping to proofread the thesis, helping take apart the second LCTV (to figure out the steps I took taking apart the first LCTV), and believing enough to throw himself on the optical segmentation dissertation stake. I also greatly appreciate (I think) the NeXT system (Dr Dennis Ruck) for making me go insane with postscript graphics in my \LaTeX document. And finally, I truly appreciate all the friends I've made at AFIT: for all their tips on one system or another. Everything's got a learning curve here; friends make the curves manageable.

I can honestly say that AFIT has made me absolutely sick in the past (due to motion sickness chair experiments), and I've had enough sleepless nights to last me sometime, but overall the AFIT education system is excellent and well worth the effort invested. If I could give the one, underlying factor that got me through the program with the positive attitude that I'm leaving with, I'd unhesitatingly say HUMOR. Humor seemed to lighten everything up and make just about any class or situation bearable.

For	
I	<input checked="" type="checkbox"/>
d	<input type="checkbox"/>
ion	<input type="checkbox"/>

Distribution/	
Availability Codes	
Dist	Avail and/or Special
A-1	



If I told my wife, Edie, and my four daughters, Mary, Cyndi, Jecka, and Katie that this thesis was for them, they wouldn't believe me, so I won't. Would you believe that I couldn't have done it without you? Okay, okay! I'll come clean. The thesis was for me, I had fun doing it, and you guys didn't. But, I am truly grateful for your support and love and understanding: for the dinners that you brought me, and for the hugs you gave me when I had to go back to school. And for all that, I dedicate this thesis to all of you.

Christopher P. Veronin

Table of Contents

	Page
Preface	ii
Table of Contents	iv
List of Figures	vii
List of Tables	x
Abstract	xi
 I. Introduction	 1-1
1.1 Problem Statement	1-1
1.2 Research Objectives	1-2
1.3 Scope	1-2
1.4 Outline of Thesis	1-2
 II. Background	 2-1
2.1 Introduction	2-1
2.2 Original Work on 2-D Gabor Transform	2-1
2.3 Texture Discrimination by Gabor Transforms	2-2
2.4 Texture "Demodulation" Using Gabor Transforms	2-4
2.5 VLSI Reverse Engineering Applications	2-6
2.6 Digital FLIR Image Segmentation	2-6
2.7 Summary	2-9
 III. Methodology	 3-1
3.1 Introduction	3-1
3.2 Application of Spatial Filtering	3-1

	Page
3.2.1 Spatial Filtering Theory	3-2
3.3 Orientation Specific Bandpass Spatial Filters	3-4
3.3.1 Pinhole Pair Filters	3-4
3.3.2 Gabor Filter CGH's	3-6
3.3.3 Real-time Filter Selection Using an LCTV	3-7
3.4 Experiment	3-11
3.4.1 Setup for Optical Segmentation	3-11
3.4.2 Input Images	3-13
3.5 Summary	3-16
IV. Results and Discussions	4-1
4.1 Introduction	4-1
4.2 Characterization of the Spatial Filters	4-1
4.2.1 3-D Intensity Profiles of Filter Images	4-1
4.2.2 Filter Spectrums	4-6
4.2.3 Comparison of Spatial Filters	4-7
4.3 Testing Results and Discussion	4-8
4.3.1 Testing With Texture Slides	4-9
4.3.2 Testing With Template Slides	4-10
4.3.3 Testing With Static FLIR Images	4-15
4.3.4 Testing With Real-Time FLIR Imagery	4-19
4.4 Summary	4-19
V. Conclusions and Recommendations	5-1
5.1 Summary	5-1
5.2 Conclusions	5-2
5.3 Recommendations	5-2

	Page
Appendix A. Detour Phase Hologram Production	A-1
A.1 Gabor Filter Program	A-1
A.2 Process and Variable Explanation	A-3
A.2.1 The Subroutine Gabor	A-4
A.2.2 Program Operation	A-5
A.3 Compiling, Previewing, Plotting, and Photoreducing	A-6
A.3.1 Compiling	A-6
A.3.2 Previewing	A-6
A.3.3 Plotting	A-6
A.3.4 Photoreducing	A-7
Appendix B. LCTV Modifications and Limitations	B-1
B.1 Introduction	B-1
B.2 LCTV Theory	B-1
B.3 Modifications	B-2
B.3.1 LCTV Disassembly	B-2
B.3.2 LCTV Assembly	B-3
B.4 LCD Configuration and Spatial Resolution Limitations	B-3
B.4.1 LCD Configuration	B-4
B.4.2 Spatial Resolution Limitations	B-5
Appendix C. Barplot Generation	C-i
C.1 Barplot Program	C-1
C.2 Explanation of Program	C-2
C.3 Output Procedures	C-3
Appendix D. Texture Plots	D-1
Bibliography	BIB-1
Vita	VITA-1

List of Figures

Figure	Page
1.1. Experimental setup for optical segmentation.	1-4
2.1. Image segmentation of anisotropic white noise texture collage.	2-2
2.2. Complete 2-D Gabor transform of the anisotropic white noise mondrian displayed in Fig. 2.1.	2-3
2.3. 2-D Fourier transforms of the Gabor elementary functions employed in one log-polar radial octave "wavelet" scheme.	2-3
2.4. a. Image of plain white cup. b. Result of summing the values measured by all filters at each region in the image.	2-4
2.5. Segmentation using two filters of different orientations.	2-5
2.6. Input image after preprocessing	2-7
2.7. Combined Gabor transforms of rotation 20, 45, 70, 110, 135, and 160 degrees	2-8
2.8. Examples of digital FLIR segmentation using Gabor transforms.	2-10
3.1. (a) Example of a 2-D cosine Gabor function (b) 2-D Fourier transform of (a)	3-2
3.2. Common setup for spatial filtering	3-3
3.3. Example of a odd impulse pair	3-8
3.4. Example of a even impulse pair	3-8
3.5. Example of a cosine Gabor detour-phase CGH negative	3-9
3.6. Example of a sine Gabor detour-phase CGH negative	3-10
3.7. Picture of the Sony Video Walkman LCTV used in the optical bench setup	3-11
3.8. Experimental setup for optical segmentation	3-12
3.9. Optical setup for observing Fourier transforms of filter designs	3-13
3.10. Complex texture image consisting of spatial frequencies of 10, 20, 30, 40, and 50 cycles/cm with its Fourier transform	3-15
3.11. Demonstration of fundamental frequency segmentation technique.	3-15

Figure	Page
4.1. (a) Pinhole pair filter image; (b) Its 3-D intensity profile	4-2
4.2. (a) Sine CGH Gabor filter image; (b) Its 3-D intensity profile	4-3
4.3. (a) Cosine CGH Gabor filter image; (b) Its 3-D intensity profile	4-4
4.4. (a) LCTV Pinhole pair filter; (b) Its 3-D intensity profile	4-5
4.5. Wavelet spectral images of pinhole filters.	4-6
4.6. Wavelet spectral images of three different filters.	4-8
4.7. Simple texture image of two orientations at 10 cycles/cm, and its Fourier transform	4-9
4.8. Segmentation of a simple texture image using a pinhole filter	4-11
4.9. Segmentation of a simple texture image using a cosine Gabor CGH filter . . .	4-11
4.10. Segmentation of a simple texture image using a sine Gabor CGH filter	4-11
4.11. Segmentation of a complex texture pattern using an pinhole pair filter	4-12
4.12. Example of segmentation of a "small" truck template slide using a single orientation pinhole pair displayed on an LCTV as a filter.	4-13
4.13. Example of a poorly segmented template slide using a pinhole filter with apertures chosen too small.	4-14
4.14. Segmentation of a truck template slide using five different pinhole filters. . .	4-14
4.15. Segmentation of a multiple object template slide using a multiple orientation pinhole filter.	4-15
4.16. Segmentation of static FLIR image REFJ16 using a pinhole filter.	4-16
4.17. Spectrum of Sony Walkman LCTV with circles drawn on top depicting a pinhole filter with 4 mm separations, 2 mm dilations, and 2 orientations	4-17
4.18. Segmentation of static FLIR image REFM13 using a pinhole filter.	4-18
4.19. Optical setup used for observing segmented and unsegmented real time FLIR images synchronously	4-20
4.20. Segmentation of two frames of real-time FLIR imagery using a circular aperture pair filter with two orientations, 0 and 90°.	4-21
A.1. Location of gaussian regions in Gabor filter holograms	A-4

Figure	Page
B.1. Sketch of magnified view of RGB pixel arrangement on the LCD. R-red; G-green; B-blue	B-4
B.2. Sketch showing composite pixel spacing components	B-6
B.3. Optical setup used to observe LCTV spectrum	B-6
B.4. Spectrum of LCTV with no input image displayed	B-7
B.5. Spectrum of LCTV with spectral coefficients from 4 cycle/cm bar pattern displayed showing lower resolution limit of LCTV.	B-8
B.6. Spectrum of LCTV with spectral coefficients from 12 cycle/cm bar pattern displayed showing upper resolution limit of LCTV.	B-9
D.1. Example of a simple texture slide with 10 cycles at two perpendicular orientations	D-2
D.2. Example of a simple texture slide with a 10 cycle background and two 20 cycle textures in parallel and perpendicular orientations	D-3
D.3. Example of a more complex simple texture slide with a 10 cycle background and three other textures consisting of 30, 40, and 50 cycles at 0, 45, 90, and 135° orientations	D-4
D.4. Example of a more complex simple texture slide with a 10 cycle background and four other textures consisting of a 20 cycle center texture and 30, 40, and 50 cycle outer lobes, all at different orientations	D-5

List of Tables

Table	Page
B.1. Mechanical Specifications of Liquid Crystal Display	B-2

Abstract

This research effort successfully implemented an automatic, optically based image segmentation scheme for locating potential targets in a cluttered FLIR image. Such a design is critical to achieve real-time segmentation and classification for machine vision applications.

The segmentation scheme used in this research was based on texture discrimination and employs orientation specific, bandpass spatial filters as its main component. The orientation specific, bandpass spatial filters designed during this research include symmetrically located circular apertures implemented on heavy, black aluminum foil; cosine and sine Gabor filters implemented with detour-phase computer generated holography photoreduced onto glass slides; and symmetrically located circular apertures implemented on a liquid crystal television (LCTV) for real-time filter selection.

The most successful design was the circular aperture pairs implemented on the aluminum foil. Segmentation was illustrated for simple and complex texture slides, glass template slides, and static and real-time FLIR imagery displayed on an LCTV.

OPTICAL IMAGE SEGMENTATION USING WAVELET FILTERING TECHNIQUES

1. Introduction

This research effort extends previous research accomplished in a 1989 thesis project titled "Gabor Transforms for Forward Looking Infrared Image Segmentation" by Kevin Ayer (3). Ayer addressed the problem of distinguishing or "segmenting" areas of interest (potential targets) from cluttered images using Gabor filtering techniques. In his thesis, the segmenting capabilities of Gabor filters were established with the use of computer algorithms and digitized images. Although Ayer's segmenting techniques were highly successful in locating potential targets, the computer algorithms used to process the images were computationally intense which severely limited the processing speed. Furthermore, orders of magnitude of additional computations would be required to process real-time images. For this reason, an optical implementation of his algorithm was proposed. A review of Ayer's research and other papers that support the segmentation capabilities of the Gabor function are presented in Chapter II.

1.1 Problem Statement

An automatic, optically based image segmentation scheme for locating potential targets in a cluttered FLIR image has never been implemented. The advantage of such a scheme is speed, i.e., the speed of light. The goal is to be able to instantaneously and automatically segment real-time FLIR images for machine vision processing. Over the past 25 years, several segmentation algorithms have been developed at AFIT (6, 15, 16, 31, 33, 34, 37), however, they are heuristic in nature and use non-linear mathematical manipulation of data—algorithms not readily implemented optically and computationally intense for real-time use (3). In contrast, image segmentation using wavelet filtering techniques can be accomplished automatically, instantaneously, and implemented

optically by using the Fourier transform and coherent image processing properties of optical lenses.

1.2 Research Objectives

This research effort was twofold. The first part focused on the design and implementation of orientation specific, bandpass spatial filters (including Gabor filters) for optical segmentation applications. The objective was to implement them for insertion in the Fourier plane of an optical correlation setup as suggested by Ayer(3). A diagram of the setup used in this research effort is shown in Figure 1.1. The inset is a representation of an orientation specific, bandpass spatial filter. The second part focused on testing the spatial filters designed for their ability to segment various input images including FLIR imagery displayed on an LCTV.

1.3 Scope

The scope of this research is given in reference to the research objectives. Three methods of implementing orientation specific, bandpass spatial filters have been attempted: 1) symmetrically located circular apertures (pinhole pair filters) implemented on heavy, black aluminum foil; 2) sine and cosine Gabor filters implemented with detour-phase computer generated holograms and photoreduced on glass slides; and, 3) pinhole pair filters displayed on a liquid crystal television (LCTV) for investigation of real-time filter selection. Methods of design and implementation are presented in Chapter III. In addition, the segmenting capabilities of the filter designs were tested using various input images. The complexity of the images ranged from simple textured patterns to static and real-time FLIR imagery displayed on an LCTV. Testing results are presented in Chapter IV.

1.4 Outline of Thesis

Chapter II provides background on previously developed digital segmentation algorithms using Gabor filtering techniques. These articles establish the segmentation capabilities of the Gabor transform, and more generally, wavelet filtering techniques. Chapter III presents the theory of spatial filtering and describes the methodology of this research effort. Implementation of each

of the three major filter designs is discussed, and details are given on the experimental setup and implementation of the various input images. Chapter IV details the results of this research effort. Characteristics of the three filter designs and the segmentation capabilities of the filters are presented and discussed. Finally, conclusions and recommendations are provided in Chapter V.

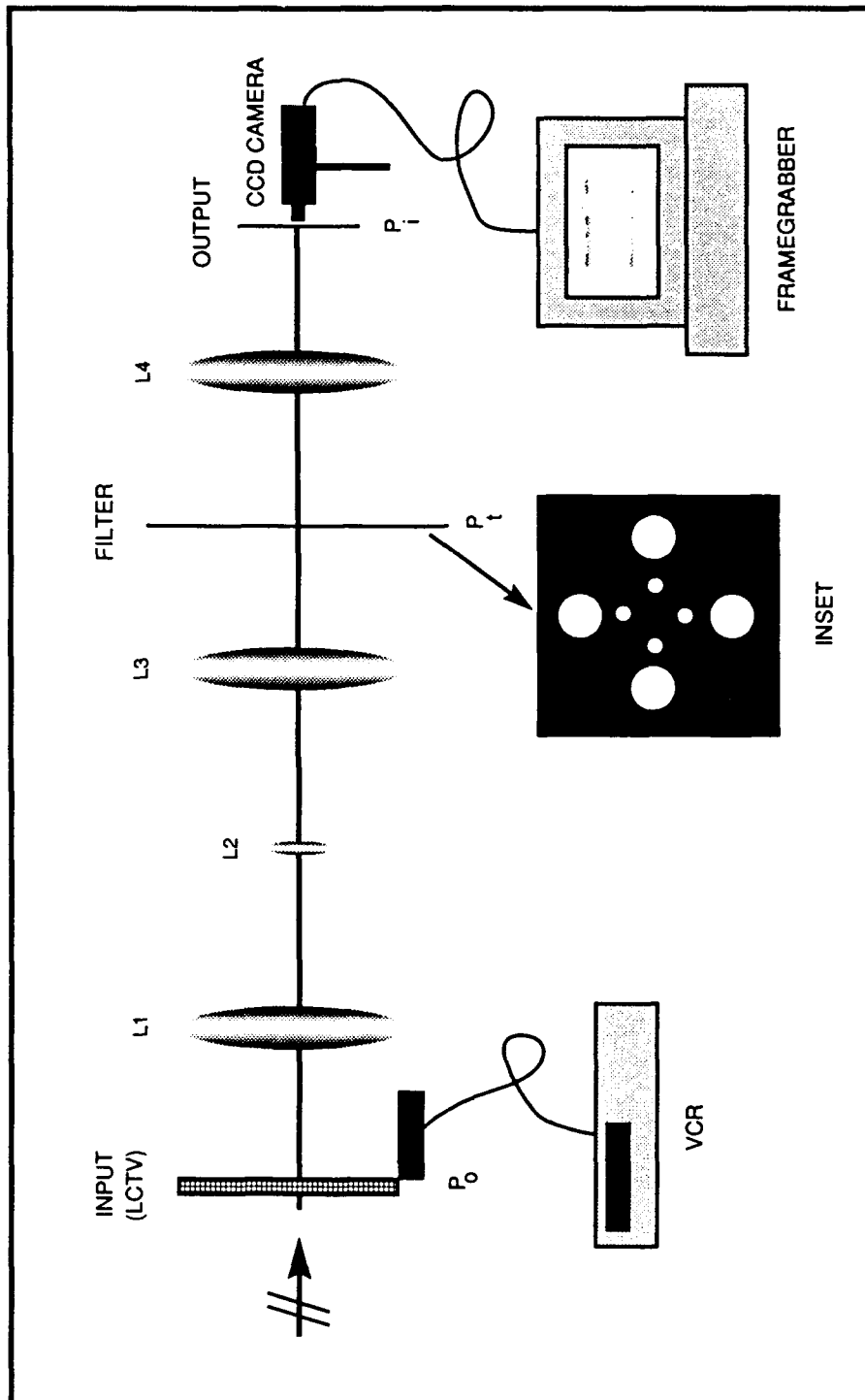


Figure 1.1. Experimental setup for optical segmentation. The inset is an orientation specific, bandpass spatial filter with circular apertures.

II. Background

2.1 Introduction

The discussion in this chapter establishes the image segmentation capabilities of the Gabor transform. To this end, five articles are reviewed which illustrate how the Gabor transform segments images. All five articles illustrate their segmentation techniques using computer algorithms and static input images. None have implemented the Gabor transform optically; however, the last article by Ayer proposes an optical implementation scheme that has been adopted in this thesis. The first three articles describe the fundamentals of texture discrimination and segmentation using the 2-D Gabor transform. Their segmentation examples show results using rudimentary textured scenes as inputs. The last two articles employ the Gabor transform to solve actual segmentation problems in the Air Force. Their segmentation examples illustrate the ability of the Gabor function to extract desired features using complex "real world" scenes as inputs.

2.2 Original Work on 2-D Gabor Transform (11)

Daugman's work with the 2-D Gabor transform has set the foundation for using the transform for texture discrimination. Since 1980, Daugman has steadily extended Gabor's original work from one dimensional Gabor filters used for information compression to two dimensional Gabor filters used for image analysis, segmentation, and compression. And, in his collaboration with Jones and Palmer, he has promoted Gabor functions as good models for two dimensional receptive fields of simple cells in the mammalian visual cortex.

In his 1988 article, Daugman illustrated the texture based image compression and segmentation capabilities of the Gabor transform using neural networks. Texture discrimination was achieved by examining the textural signature of an image using the Gabor transforms of the image and grouping similar Gabor coefficients together. An illustration of this is given in Figures 2.1 and 2.2.

In this same article, Daugman also proposed simplified versions of the Gabor function by eliminating two degrees of freedom. He called these functions "self similar" Gabor functions. In his "biologically motivated" implementation of these functions called the log-polar set, the gaussian dilations and sinusoidal frequencies are distributed in octave steps and six orientations

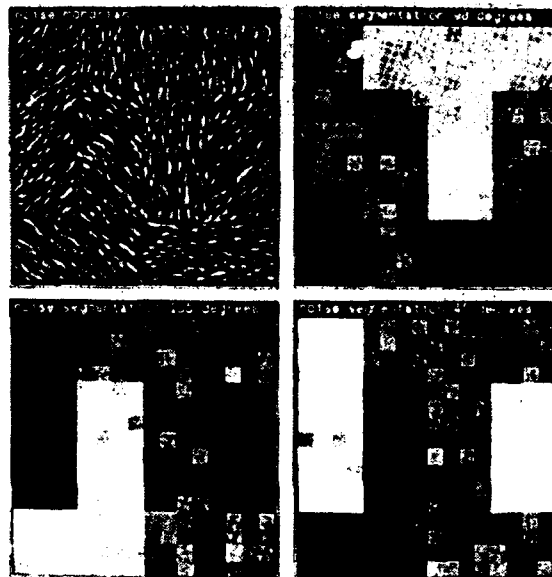


Figure 2.1. Image segmentation of anisotropic white noise texture collage (upperleft), by the dipole clustering of coefficients in the complete 2-D Gabor transform displayed in Fig. 2.2.

are used differing in 30° steps. This configuration, shown in Figure 2.3, appears to be a good organization for spatial filters attempting multiple frequency and orientation segmentation.

2.3 *Texture Discrimination by Gabor Transforms*(38)

In 1986, Turner wrote an article supporting the Gabor transform as a good model for "preattentive texture discrimination" in visual neuron performance. In other words, his results suggested that Gabor transforms might be good models for spontaneous texture segmentation in the human visual system. His work was based to a large degree on the work of Daugman, Jones, and Palmer up through 1985.

In his article, a series of programs was created to evaluate the applicability of Gabor functions to texture analysis. Three types of images were used as inputs. They were characterized by "the statistical complexity which distinguishes the different textured regions," and were classified as first-order, second-order, and third-order differences. It was shown that, when properly applied, Gabor functions were able to distinguish the textured regions of the images by

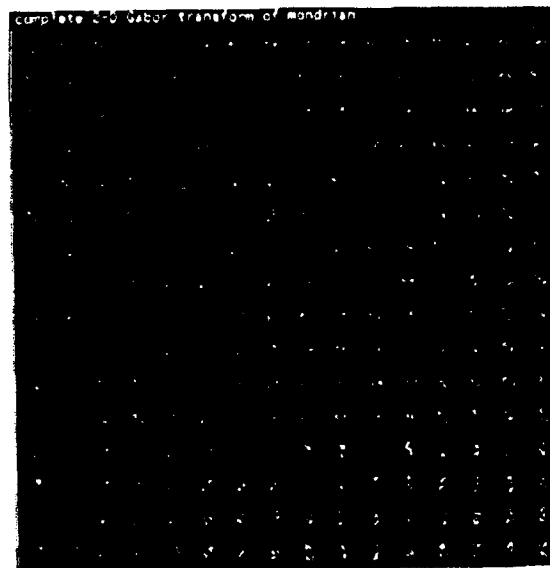


Figure 2.2. Complete 2-D Gabor transform of the anisotropic white noise mondrian displayed in Fig. 2.1. Different local spectral dipoles are apparent in regions of the transform corresponding to regions of the image described by different anisotropic texture moments.

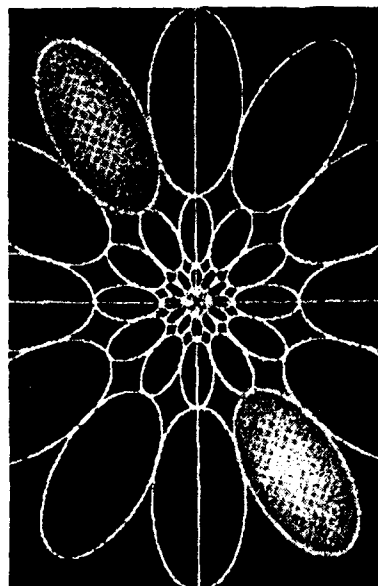


Figure 2.3. 2-D Fourier transforms of the Gabor elementary functions employed in one log-polar radial octave "wavelet" scheme.

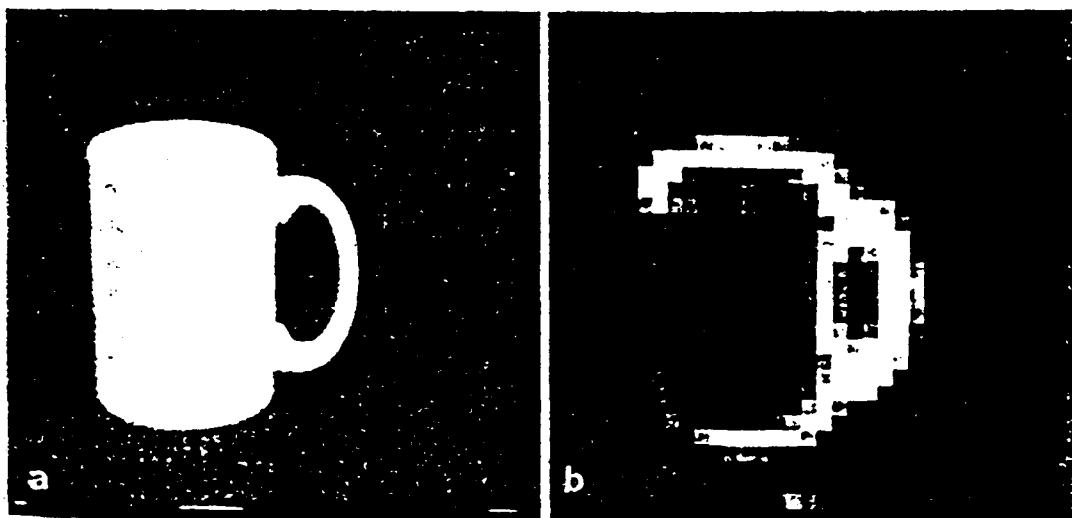


Figure 2.4. a. Image of plain white cup. b. Result of summing the values measured by all filters at each region in the image.

successively reducing the statistical complexity of the images to “first-order differences in the measured values.” Turner asserts that an automatic segmentor can be developed based on the successive reapplication of Gabor functions to textured images. He concluded that, based on his results, Gabor functions can be used to discriminate textures in an image. The orientation specific, bandpass spatial filters presented in this thesis can simultaneously apply multiple orientation, frequency, and dilation filtering to the input images and, hence, act as automatic segmentors. An example of Turner’s results using first-order statistics is given in Figure 2.4.

2.4 Texture “Demodulation” Using Gabor Transforms(5)

In their 1990 article, Bovik, Clark, and Geisler characterized image texture as a “carrier of region information” similar to how a communications signal is modulated for transmission. In this sense, they characterized the Gabor transform as a demodulating function which filters the regional information from the image texture. They liken this demodulation technique to “tuning” the orientation, radial frequency bandwidth (dilation), and center frequency of the 2-D Gabor function to a specific image texture.

Due to computation limitations, only a small number of filters could be employed in

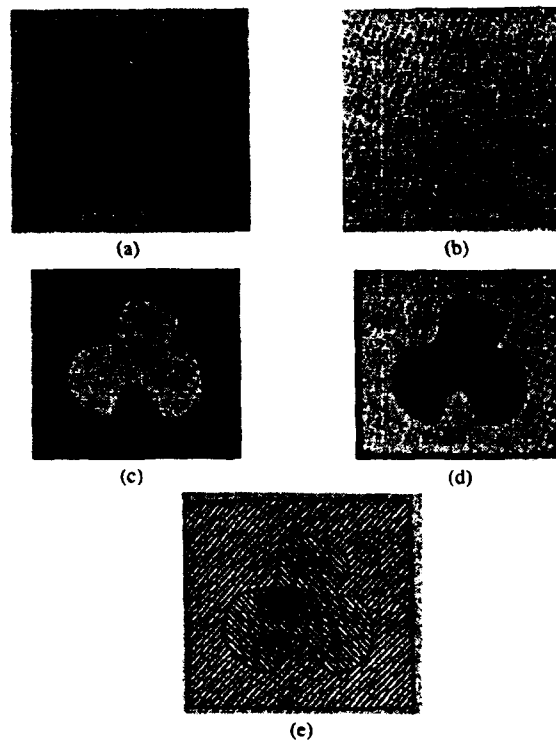


Figure 2.5. Segmentation using two filters of different orientations: a. original; b. Fourier transform; c.,d. channel amplitudes recovered; e. computed texture boundaries.

their algorithm at one time. Thus, guidelines were given for filter selection based on a simple peak-finding algorithm applied to the image power spectrum. Using these guidelines, a "computer vision" model was developed and applied to both synthetically generated and naturally occurring textures. An example of their segmentation results is given in Figure 2.5.

Although this technique did not select an optimal Gabor filter set, their results demonstrated the ability of the Gabor transform to achieve segmentation using only a subset of the information within each texture. They concluded that the Gabor transform is a "feasible approach to segmenting image texture in a predictable manner" and proposed that new algorithms should be developed for using the Gabor transform for edge and motion detection. However, they deemed the "most difficult problem" to be the "development of fast algorithms and architectures for filtering an image to a large set of Gabor filters" due to computation limitations. Indeed, speed limitations are major obstacles for computer based algorithms, but they pose no problem for optically based

algorithms like the one developed in this thesis.

2.5 VLSI Reverse Engineering Applications (28)

In his 1989 thesis, Mueller employed Gabor transforms to segment out the contacts in VLSI circuits to assist in reverse engineering the circuits. The VLSI circuit diagrams were digitized using a camera and a video image processing board. Mueller used computer algorithms for processing all the image information including the Gabor transforms. Before segmentation processing, the images were preprocessed by normalizing the brightness of the individual image pixels and enhancing their contrasts.

Various combinations of orientations, pitch, and frequency of Gabor functions were investigated, and guidelines were developed for their use. An interesting result was Mueller's choice of orientations for his Gabor filters. Because the contacts were circular, all orientations of the Gabor filter should be equally likely to segment the contacts from the background features. However, because most of the other features in the VLSI circuit (which he did not desire to segment) were oriented at angles of 0 and 90, these two common orientations were not used. Consequently, he chose the orientations at angles of 20, 45, 70, 110, 135, and 160 in order to equalize the spacing between rotations and achieved excellent results. He concluded that "Gabor processing is a viable technique for contact segmentation." An example of his results is shown in Figures 2.6 and 2.7.

2.6 Digital FLIR Image Segmentation (3)

In his 1989 thesis, Ayer employed Gabor transforms to segment out targets in cluttered Forward Looking InfraRed (FLIR) images. He used computer algorithms for processing all the image information including the Gabor transform. The FLIR images were preprocessed before segmentation by normalizing the brightness of the image pixel values and post-processed by thresholding and binarizing the pixel values.

Both sine and cosine Gabor functions were investigated for their segmentation abilities in Ayer's research. To this end, he demonstrated that sine Gabor functions act as "edge detectors" and cosine Gabor functions act as "body fillers." He used orientations of 0, 45, 90, and 135

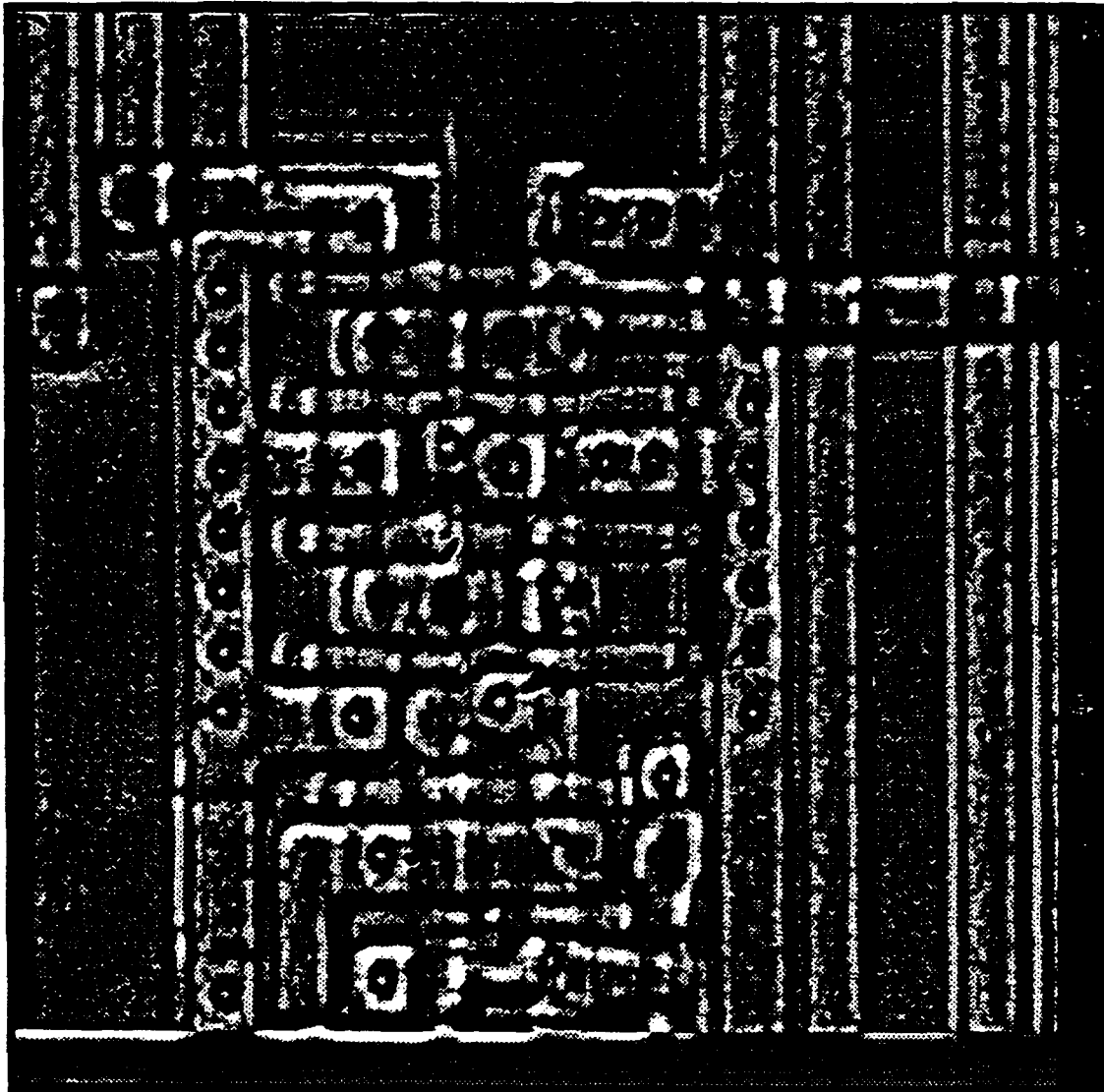


Figure 2.6. Input image after preprocessing

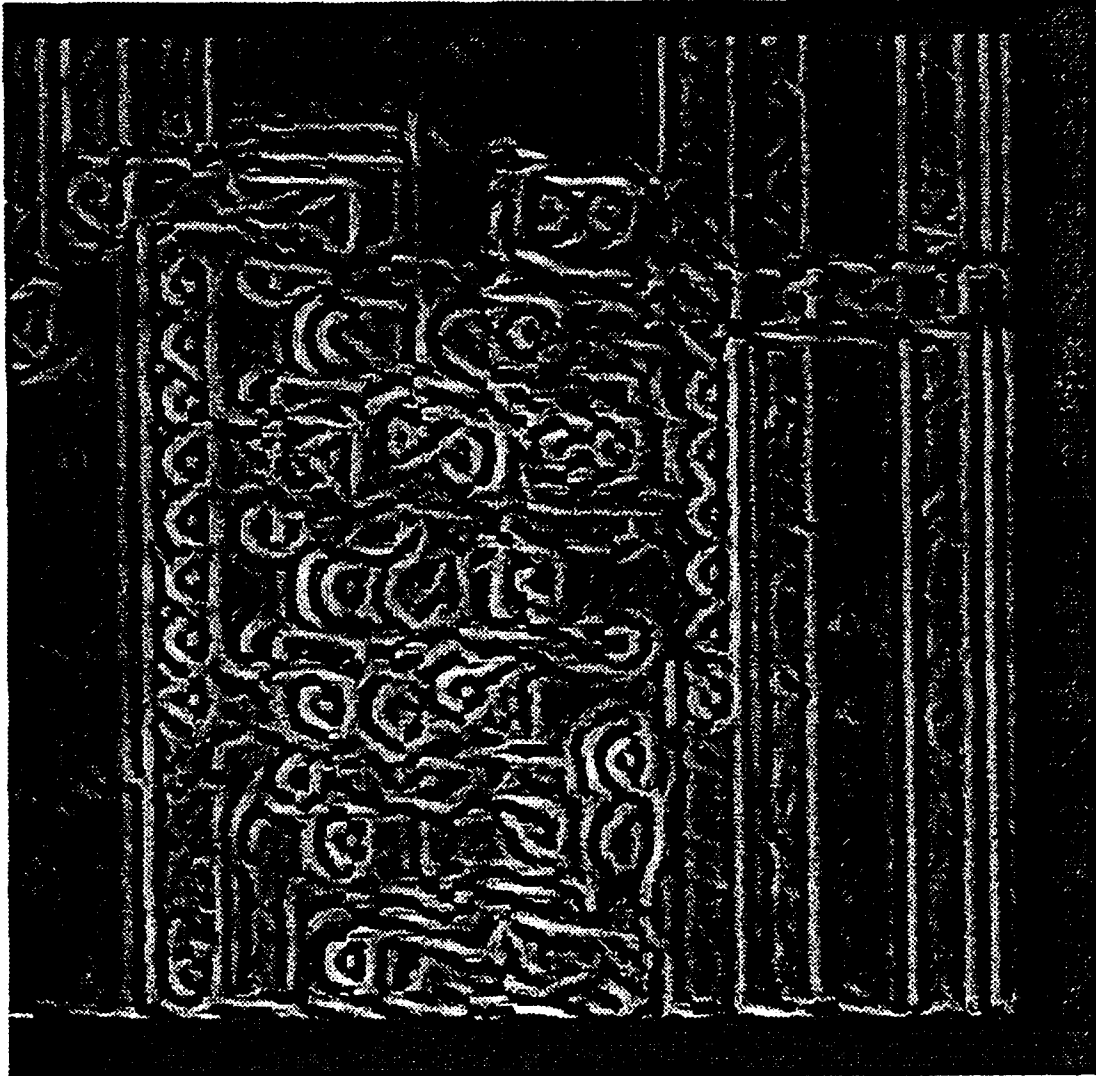


Figure 2.7. Combined Gabor transforms of rotation 20, 45, 70, 110, 135, and 160 degrees

degrees, because these were the orientations most prevalent in the targets. He concluded that "in combination, sine and cosine Gabor functions produce fully segmented targets" from the cluttered FLIR images. Binarized images segmented using his techniques are shown in Figure 2.8.

Ayer also proposed an optical implementation scheme for segmenting images using Gabor transforms which was adopted in this research. His scheme was based on implementing Gabor filters as computer generated holograms and using spatial filtering techniques to segment the images.

2.7 Summary

The five articles reviewed established the digital segmentation capability of the Gabor transform using computer algorithms and static images. They all base their findings on the ability of the transform to discriminate between texture frequency, orientation, and localization. Daugman and Turner's use of the Gabor transform was biologically motivated. They see the transform as a possible answer to modeling the perceptive field of a cortical neuron. Bovik, et al., applied the Gabor transform as a spatial filter and provided insight into efficient filter selection. Mueller and Ayer provided successful illustrations of segmentation using the Gabor transform applied to real world problems. However, all were limited in speed due to relatively slow digital computations of 2-D Fast Fourier Transforms (FFTs) and were unable to segment real-time imagery. The optical algorithm developed in this thesis is capable of instantaneous 2-D FFTs which makes it perfectly suited for segmenting real-time imagery.

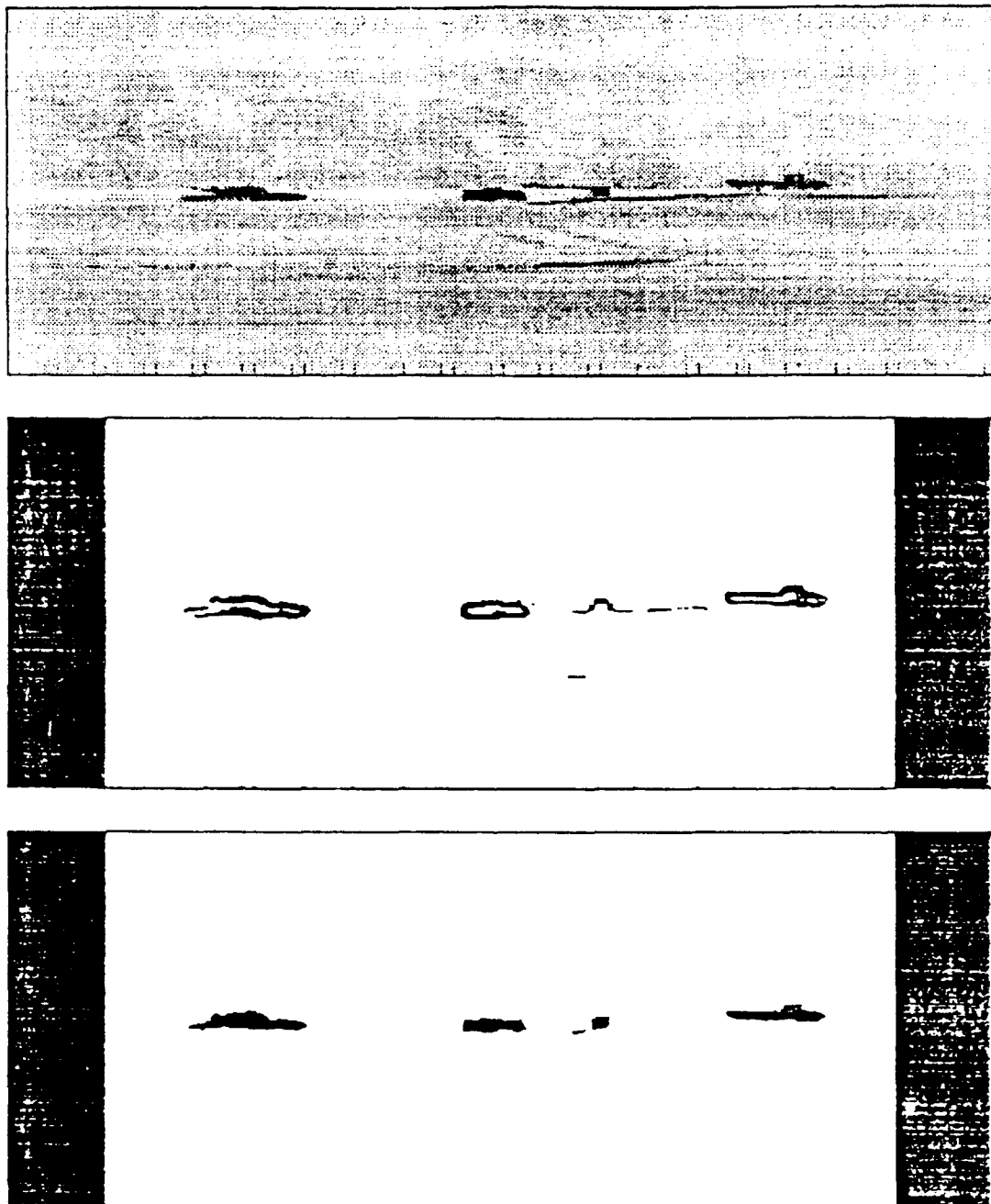


Figure 2.8. Examples of digital FLIR segmentation using Gabor transforms. Original FLIR image (top); Binary version of sine Gabor transform of top image: edge detection (middle); and Binary version of cosine Gabor transform of top image: body filling (bottom)

III. Methodology

3.1 Introduction

The discussion in this chapter outlines the theory of optical spatial filtering and methods of implementation and testing of optical spatial filters as applied to texture discrimination and image segmentation. Chapter organization is divided into three parts. The first part focuses on the theory of optical spatial filtering and its application to texture discrimination. The second part focuses on the design and implementation of texture discriminate optical spatial filters. Implementations of these filters included simple pinholes punched in heavy, black aluminum foil, computer generated holograms (CGH's) of sine and cosine Gabor filters, and pinhole pairs displayed on a liquid crystal television (LCTV). The third part focuses on the design and implementation of the optical bench setup and a variety of input images used to test the optical spatial filters. Complexity of the input images ranged from simple textures on glass slides to real-time FLIR imagery displayed on an LCTV. The results from these tests are described and discussed in Chapter IV.

3.2 Application of Spatial Filtering

Spatial filtering is used to *optically* implement the segmentation algorithms presented in the Ayer thesis (3). Ayer's underlying methodology was to segment the objects in an input image by correlating Gabor filters with the input image. He *digitally* implemented the Gabor filters and the input image in the *space domain*, computed their fast Fourier transforms (FFT's), multiplied the two FFT's together, and then computed the inverse FFT of the product. To achieve multiple orientation, frequency, and dilation filtering, correlation intensities resulting from computations with a filter at a single orientation, frequency, and dilation were added together – analogous to *incoherent* imaging (linear in intensity).

Although the underlying methodology of this thesis remains the same as the Ayer thesis, the optical filters used were implemented in the *frequency domain* rather than the space domain. Because the algorithm was implemented using *coherent* imaging, individual correlations must be added together on a complex amplitude basis. Thus, multiple orientation, frequency, and dilation filtering was realized with a single spatial filter implemented in the frequency domain (linear in

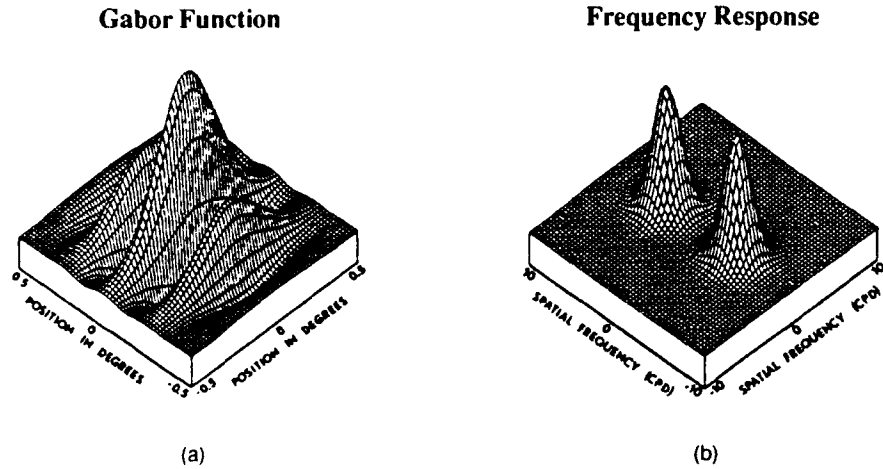


Figure 3.1. (a) Example of a 2-D cosine Gabor function (b) 2-D Fourier transform of (a)

complex amplitude). An example of a 2-D cosine Gabor function (space domain) and its 2-D Fourier transform (frequency domain) is given in Figure 3.1 (11).

3.2.1 Spatial Filtering Theory In this thesis, two-dimensional Fourier transforms are used to resolve an input image into its spectrum: a set of paired Fourier coefficients that represent a system of sine and cosine functions which contain all the information of the original image. Each coefficient pair represents a specific spatial frequency and orientation at some amplitude and phase.

In optical image processing, *spatial filtering* implies physically obstructing or modifying a portion of the spectrum of the input image. The most common setup for optical spatial filtering in a coherent imaging system is shown in Figure 3.2.

In this setup, called a $4-f$ setup, collimated light from a laser acts as a plane wave source incident on an input image (object) located at P_o . The transform lens, L_t , performs a two-dimensional Fourier transform of the object which is focused at P_t . The “inverse” transform lens, L_i , performs a two-dimensional “inverse” Fourier transform of the spectrum at P_t which is focused at P_i . If no spatial filter is placed at P_t , the output image at P_i is the same as the input image with some scaling depending on the focal lengths of the lenses and with some blurring depending on the diameters of the lenses. However, if a portion of the spectrum is obstructed by a

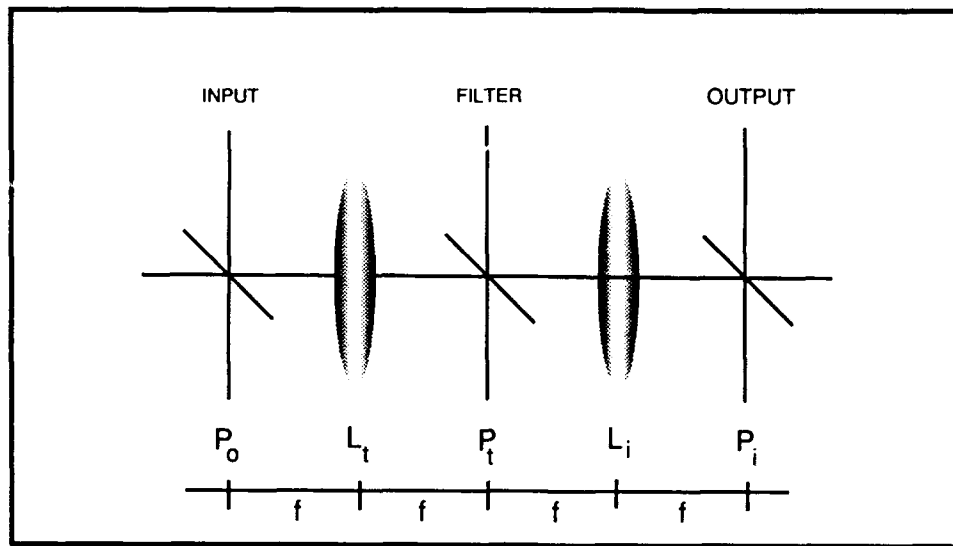


Figure 3.2. Common setup for spatial filtering

spatial filter, the output image can be altered in significant ways (13:87, 141, 167).

Mathematically, spatial filtering in a coherent imaging system can be represented as a two-dimensional convolution between the input image and the inverse Fourier transform of the spatial filter. Goodman (13:166) derived this convolution relationship for the intensity distribution of a 4- f system:

$$I(x_i, y_i) = K \left| \int_{-\infty}^{\infty} \int_{-\infty}^{\infty} g(\xi, \eta) h(x_i - \xi, y_i - \eta) d\xi d\eta \right|^2 \quad (3.1)$$

where, K is a constant, g represents a space-varying amplitude transmittance function of the input image at P_o , and h represents the inverse Fourier transform of the space-varying amplitude transmittance function of the spatial filter at P_t . Note that if h is given by

$$h(x, y) = s^*(-x, -y) \quad (3.2)$$

then the relationship can be thought of as the crosscorrelation of g and s (13:178).

3.3 Orientation Specific Bandpass Spatial Filters

The segmentation filters designed in this thesis can be classified as orientation specific band-pass spatial filters. Orientation specific bandpass spatial filtering implies frequency discrimination or “textural” discrimination at a specific orientation of the texture. According to Bovik, et.al. (5), textures can be modeled as “irradiance patterns distinguished by a high concentration of localized spatial frequencies.” Where “distinct textures are characterized as differing significantly in their dominant spatial frequencies.” Thus, optically segmenting distinct textures should only require passing their dominant spatial frequencies through symmetric apertures at appropriate separations and orientations and blocking out the rest of the spectrum. Now the question is raised: how can one determine the dominant spatial frequencies of a group of textures or an input image?

Bovik provided a simple way to choose dominant frequencies when an image contained two discriminable texture regions based on the following criteria: “For strongly oriented textures, the most significant spectral peak along the orientation was chosen [as the dominant frequency]. For periodic textures, the lower fundamental frequency was chosen [as the dominant frequency]. Finally, for non-oriented textures, the center [dominant] frequencies were chosen from the two largest maxima (5).” This research effort identified dominant spatial frequencies in a similar manner to Bovik’s method by simply looking at the spectrum for the brightest spectral peak(s) (other than DC) along a specific orientation.

Of course, the apertures chosen to pass the spatial frequency components were *gaussian* pairs, i.e., Fourier transforms of Gabor functions. However, due to ease of implementation, *pinhole* pairs were initially used to demonstrate coarse texture segmentation. The implementation of both the pinhole pairs and the gaussian pairs are described in the following paragraphs.

3.3.1 Pinhole Pair Filters Pinhole pair filters are nothing more than symmetrically located circular apertures. In the space domain, one could think of them as Airy disc wavelets. In other words, if we model the circular apertures as having constant intensity across them, then the transmittance function of a symmetric aperture pair can be expressed mathematically in the frequency domain as:

$$T(\xi, \eta) = \text{circ}\left(\frac{\rho}{(l/2)}\right) * [\delta(\xi - \xi_0, \eta - \eta_0) + \delta(\xi + \xi_0, \eta + \eta_0)] \quad (3.3)$$

where:

$$\text{circ}\left(\frac{\rho}{(l/2)}\right) = \begin{cases} 1 & \rho \leq l/2 \\ 0 & \text{otherwise} \end{cases} \quad (3.4)$$

“*” represents a convolution, δ represents a delta function, $\rho = \sqrt{\xi^2 + \eta^2}$, ξ_0 represents a distance along the ξ direction, η_0 represents a distance along the η direction, and l represents the pinhole dilation (diameter).

Thus, the “inverse” Fourier transform of the symmetric aperture pair can be expressed mathematically in the space domain as an Airy disc wavelet:

$$t(x, y) = \left(\frac{l}{2}\right)^2 \frac{\mathbf{J}_1(\pi l r)}{(l r/2)} \cos(2\pi(\xi_0 x + \eta_0 y)) \quad (3.5)$$

where, $r = \sqrt{x^2 + y^2}$ and \mathbf{J}_1 represents a first-order Bessel function.

Furthermore, Goodman (13:66) derived the intensity of an Airy disc which, combined with the square of the sinusoid, gives the intensity function of the Airy disc wavelet:

$$I(x, y) = |t(x, y)|^2 = \left[2 \frac{\mathbf{J}_1(\pi l r / \lambda f)}{(\pi l r / \lambda f)}\right]^2 0.5 [1 + \cos(2\pi[2\xi_0(x + y)])] \quad (3.6)$$

where it was assumed that $\xi_0 = \eta_0$.

Using Equation 3.6, the number of cycles in the middle lobe of the Airy disc can be predicted. If r_0 is the distance from the origin to the first zero crossing of the Airy disc, then

$$r_0 = \frac{1.22\lambda f}{l} \quad (3.7)$$

Additionally, the spatial frequency of the wavelet can be given in terms of

$$2\xi_0 = \frac{2\rho}{\lambda f} \quad (3.8)$$

Thus, the number of cycles over the total lobe can be calculated from Equations 3.7 and 3.8 as:

$$\frac{\text{\#cycles}}{\text{centerlobe}} = 2r_0 2\xi_0 = \frac{4.88\rho}{l} \quad (3.9)$$

For example, if the aperture separation is 2 mm ($\rho = 1$ mm) and the aperture dilation, l , is 1 mm, then the number of cycles per middle Airy disc lobe should be 4.88 cycles/lobe. Note that this result is independent of the wavelength of the laser light or the focal length of the lens.

The implementation of the pinhole pair filters was trivial and only required that some medium be placed in the filter plane that could be impressed with small circular apertures (pinholes) to pass the desired spectral coefficients and block the rest of the image spectrum. The medium of choice was heavy, black aluminum foil, since it was readily available, required no special tools or software to manipulate (i.e., drill press or computer), and retained its shape fairly well (some slight microscopic tearing was unavoidable). The filters were made by cutting and smoothing 5 cm x 5 cm pieces of foil, then impressing circular aperture pairs into them using a pin. The apertures were placed along a common axis symmetrical to an origin (middle of the foil). Separations of apertures varied from 2 mm to 12 mm. Diameters of apertures varied from about .5 mm to 3 mm. Orientations were not limited since the filters were placed in a rotating mount with a 360° range. Characteristics of the pinhole pair filters are given in Chapter IV.

3.3.2 Gabor Filter CGH's Like the pinhole pair filters, Gabor filters are gaussian aperture pairs placed along a common axis symmetric to some origin. However, creating the gaussian apertures was not trivial. Three general methods of implementing the gaussian apertures were determined feasible. These methods were 1) encode the gaussians mathematically into detour-phase computer generated holographs (CGH's), output the holographs onto transparencies, and photoreduce onto glass slides. 2) Coherently image a gaussian apodizer (obtained from Lt Col James Mills (26)) onto either glass slides or thermal plastic using two lens imaging and a translatable mount. 3) Create grey-scale gaussian filters on the computer, output to transparencies, and photoreduce onto glass slides.

Due to time restraints, only the detour-phase CGH method of implementing the Gabor filters was pursued. The advantage of detour-phase CGH's over the other two methods was the availability of a detour-phase CGH program that had already been written by a previous AFIT student, Vicky Robinson (32). Although modification of the program was necessary, at least some precedent had been set for implementation of the holograms. A good explanation of the theory behind detour-phase holography applied toward amplitude holograms can be found in the

Robinson thesis or in Reference (21).

The CGH program written to generate Gabor filters in the frequency domain makes a distinction between sine and cosine Gabor functions. Recall that a simple sine function in the space domain can be represented in the frequency domain by an odd impulse pair, Figure 3.3, and a simple cosine function in the space domain can be represented in the frequency domain by an even impulse pair, Figure 3.4 (12). Thus, a single frequency, single orientation cosine Gabor filter can be realized by two symmetrically located gaussian apertures of equal transmittance with their background set as close to zero as possible (recall Figure 3.1b). However, in order to realize a similar sine Gabor filter, its background must be shifted up from zero by half the amplitude of the positive part so that the peak of the negative part has zero transmittance, and the net effect is an odd gaussian pair with an incorporated DC bias.

A detailed description of the CGH program used, output procedures, and photoreduction procedures followed in making the CGH's are given in Appendix A. The program produces the "negative" of the desired output, because the photoreduction process reverses the image. Examples of sine and cosine Gabor detour-phase CGH negatives are given in Figures 3.5 and 3.6. Characteristics of the Gabor filters and comparisons to pinhole pair filters are given in Chapter IV.

3.3.3 Real-time Filter Selection Using an LCTV A Sony Video Walkman liquid crystal television (LCTV) with a built-in 8 mm VCR was used as an amplitude spatial light modulator (SLM) for investigating real-time display of spatial filters and input images in the optical bench setup. The LCTV used is pictured in Figure 3.7. This section describes how the pinhole filters were displayed on the LCTV. Section 3.4.2 describes how the input images were displayed on the LCTV.

Pinhole pairs were displayed on the LCTV by the use of a Panasonic Video Camera on a tripod mount. The video output of the camera was connected to the video input of the LCTV with the LCTV switched to "line" mode. Pinholes were impressed into black aluminum foil and backlit by a directional white light source. The camera was then focused onto various separations of pinholes until the desired combination was found. A 2.5:1 ratio of pinhole separation distance on foil to pinhole separation distance on the LCTV was observed. For example, a 5 mm separation on the aluminum foil corresponded to a 2 mm separation on the LCTV.

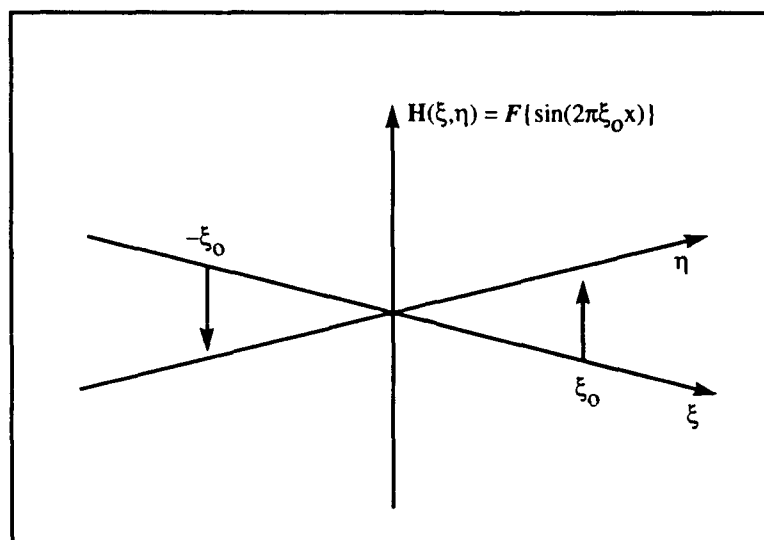


Figure 3.3. Example of a odd impulse pair

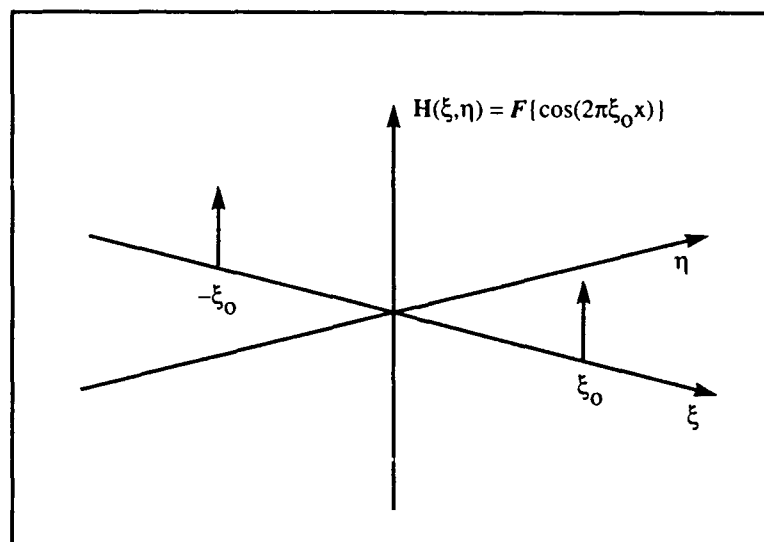


Figure 3.4. Example of a even impulse pair

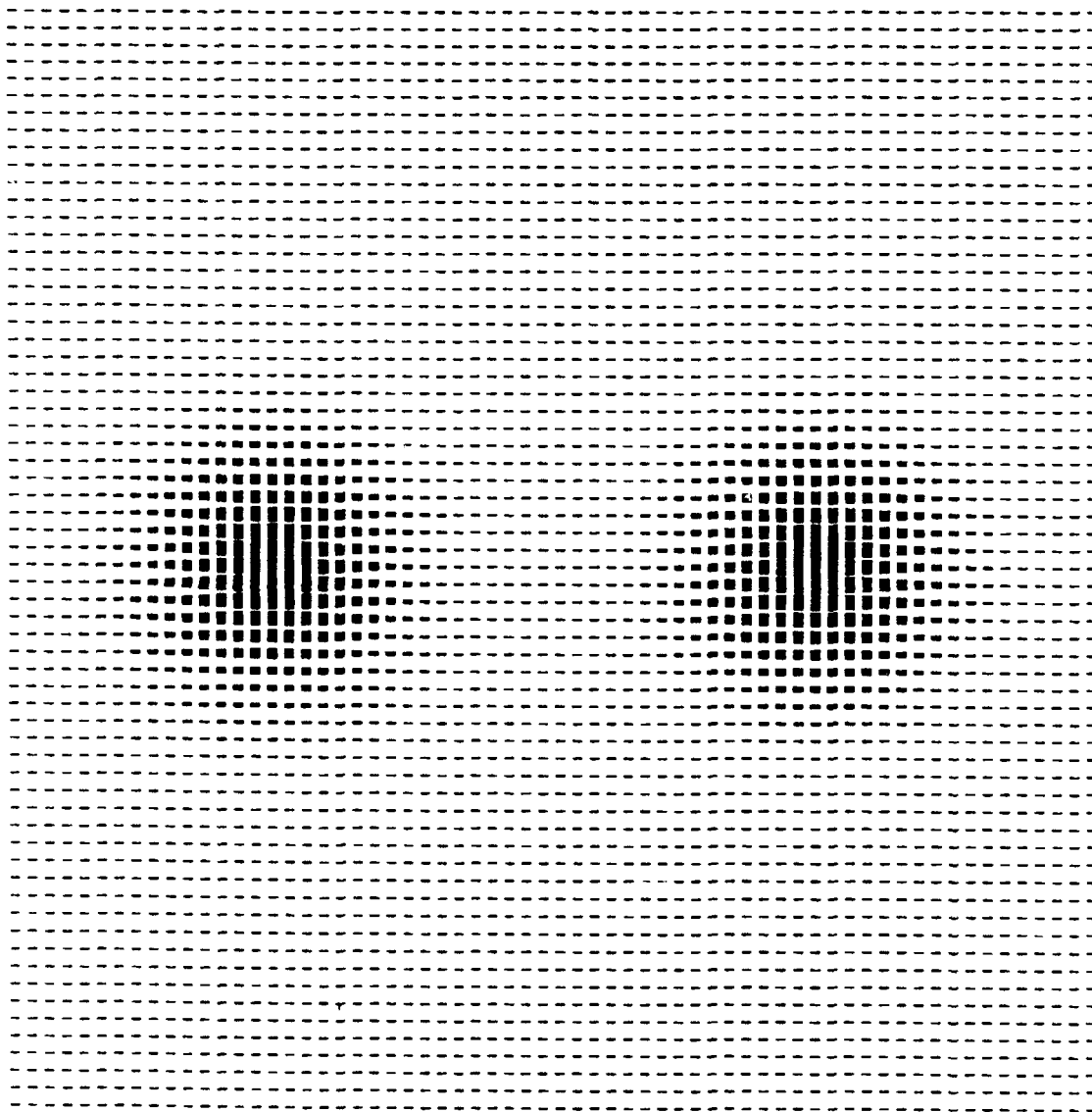


Figure 3.5. Example of a cosine Gabor detour-phase CGH negative

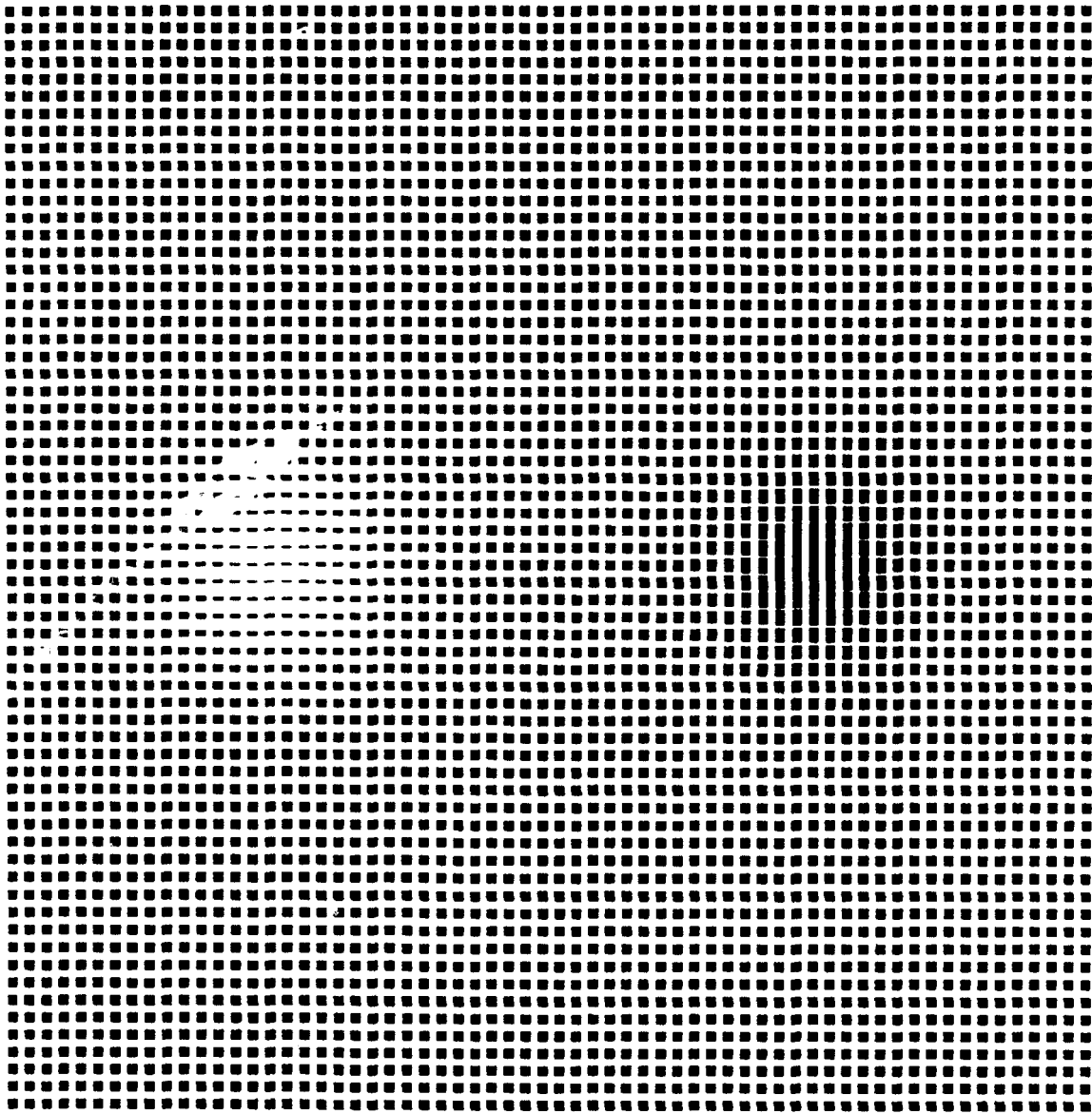


Figure 3.6. Example of a sine Gabor detour-phase CGH negative

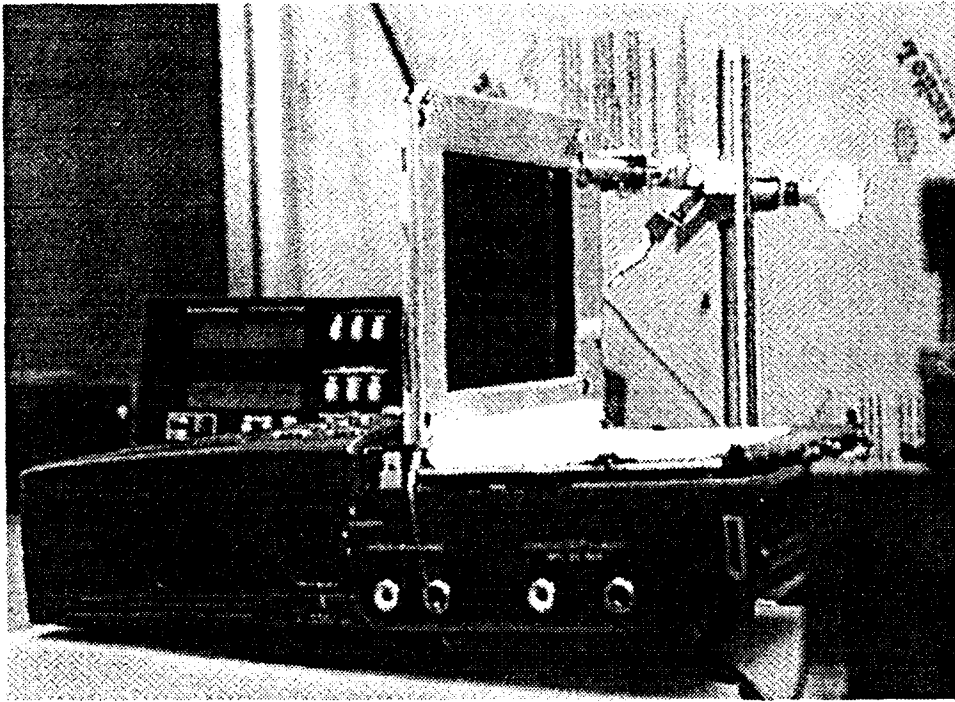


Figure 3.7. Picture of the Sony Video Walkman LCTV used in the optical bench setup

Specifications of the LCTV and details of the modifications necessary for use in the optical bench setup are given in Appendix B. Characteristics of the pinhole filters displayed on the LCTV are given in Chapter IV.

3.4 Experiment

This section describes the experimental setup used for optical segmentation and explains the design and implementation of the input images used for testing the three spatial filter designs.

3.4.1 Setup for Optical Segmentation The basic setup used to perform optical segmentation in this thesis is given in Figure 3.8. Input images were placed at P_o , and spatial filters were placed at P_f . The only difference between this setup and the general spatial filtering setup shown in Figure 3.2 is two extra lenses which increase the size of the input image spectrum incident on the spatial filter at P_f . Hence, this setup could be called an $8-f$ setup. An increase in the spectrum size allows the individual spatial frequencies (diffraction orders) to be identified and segmented

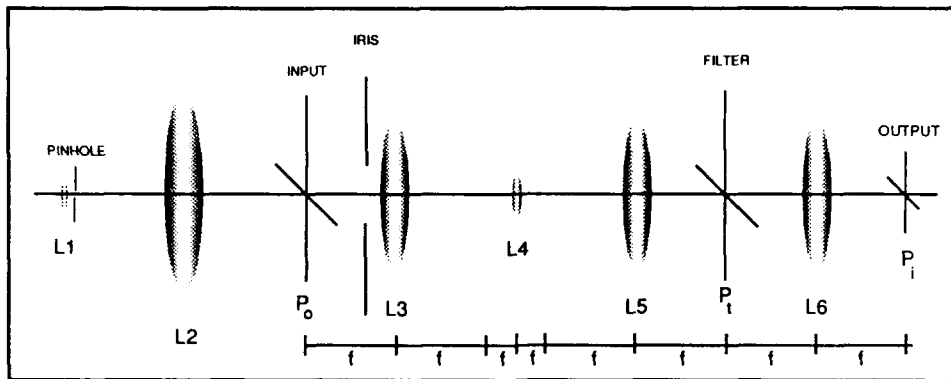


Figure 3.8. Experimental setup for optical segmentation

more easily. For example, the relationship between input image spatial frequency and spectrum location in the x -direction is

$$f_x = x_f / \lambda f \quad (3.10)$$

where f_x is the x -component of the spatial frequency, x_f is the x -component of the spectrum location, λ is the wavelength of the source, and f is the focal length of the lens. Thus, if $f_x = 10$ cycles/cm, $\lambda = 488.0$ nm, and $f = 300$ mm, then $x_f = 0.146$ mm, which is physically too small to segment easily. However, if we magnify x_f , say $7.5x$, it has a dimension of 1.01 mm, which is more easily segmented.

Although a variety of lenses were used at different times during the research, the basic configuration shown in Figure 3.8 remained the same. An argon-ion laser ($\lambda = 488.0$ nm) was used for the coherent light source. The beam was collimated to a 3 1/2 inch diameter with a 10x microscope objective, a 15 μ m pinhole, and a 150 mm, 5 1/2 inch lens in order to use as much of the LCTV screen as possible (the LCTV had a 4 inch diagonal screen). The final setup configuration used for taking all the data presented in the thesis had 300 mm compound lenses for L_3 , L_5 , and L_6 , and a simple 40 mm convex lens for L_4 . Thus, the magnification of the spectrum was $7.5x$. The iris served as an aperture stop and cut down on the high frequency interference between pixels when the LCTV was used as an input device. A Sony CCD camera was placed at P_i to record the output images. The camera was connected to a TARGA framegrabber in a Zenith 286 computer. Also, because L_3 and L_5 were similar lenses, the Fourier transform of the spatial

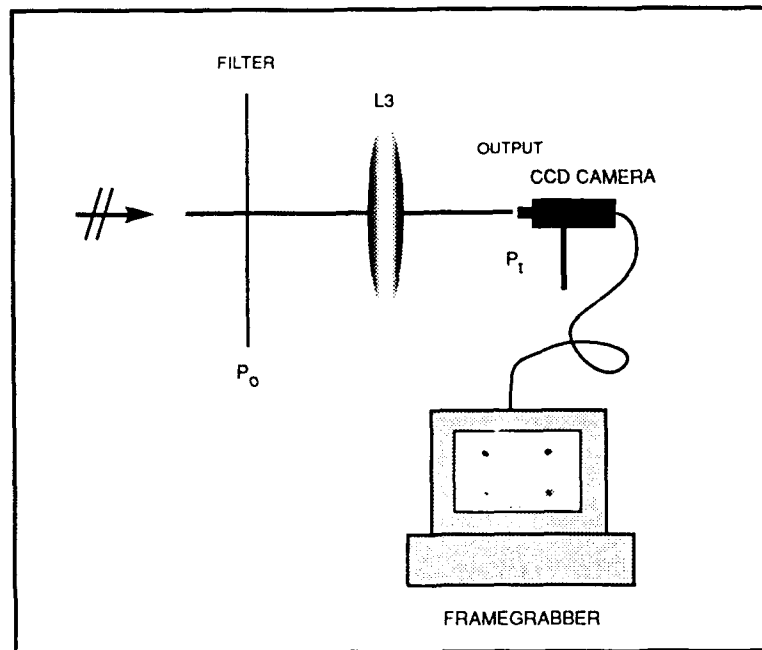


Figure 3.9. Optical setup for observing Fourier transforms of filter designs

filters could be recorded without changing the basic configuration. This was done by placing a filter at P_o and observing the Fourier transform of the filter with the CCD camera at P_t (see Figure 3.9).

3.4.2 Input Images Input images varied from simple line textures to static and real-time FLIR images displayed on an LCTV. The primary purpose of the input images was for testing the spatial filters and determining the optimum filter designs and configurations.

3.4.2.1 Texture Slides The input texture slides were made to test the spatial filters for simple texture segmentation. The texture slides contained combinations of bar pattern frequencies of 10, 20, 30, 40, and 50 cycles/cm. These frequencies were considered to be the "fundamental" spatial frequencies of the texture slides.

The methodology for segmenting a bar pattern was based on passing the fundamental or first-order spectral coefficients (symmetrically paired) corresponding to the fundamental frequency of the bar pattern. Using Equation 3.10 and taking into account the $7.5x$ spectrum magnification,

the separations of the first-order spectral coefficients, $2x_f$, were calculated to be approximately 2.2, 4.4, 6.6, 8.8, and 11 mm, respectively.

For example, the irregular texture pattern shown with its Fourier transform in Figure 3.10 consists of spatial frequencies of 20, 30, 40, and 50 cycles/cm set against a background of 10 cycles/cm. Using the fundamental frequency methodology for segmenting the irregular pattern from the background would entail passing the first-order spectral coefficients circled in Figure 3.11 and blocking the rest of the spectrum. The results of segmenting the texture slides are presented in Chapter IV.

The texture slides were made by modifying the CGH FORTRAN code given in Appendix A to generate bar plots of various frequencies. Next, some "cut and paste" was performed on the output plots, and the results were transferred to transparencies with a photocopier. Finally, the transparencies were photoreduced by 20x to a 1 cm x 1 cm size on glass slides. The FORTRAN code used to generate the bar plots is given in Appendix C; texture plots are shown in Appendix D.

3.4.2.2 Template Slides The next level of segmentation testing involved segmenting simple shapes and objects (silhouettes) of constant irradiance and no background clutter. Although the template slides are essentially "pre-segmented", they were the next logical step to segmenting FLIR images by helping to calibrate and optimize the aperture spacings and dilations. This was accomplished using template slides of large and small squares, circles, triangles, letters, tanks, trucks, and F-15's. These slides were already available in the lab from previous experiments, and no modifications were necessary. The results of segmenting the texture slides are presented in Chapter IV.

3.4.2.3 Static FLIR Images on an LCTV The static FLIR input images were used to test the spatial filters for their ability to segment objects in cluttered background. The FLIR images segmented were the REFJ series and REFM series, which were the same ones used by Ayer (3). An LCTV SLM was used as the input medium for the static FLIR images in order to lay the ground work for inputting real-time FLIR images. Although the resolution of the LCTV is poor compared to other SLMs, the requirement for grey-scale capability in real-time necessitated the use of the LCTV.

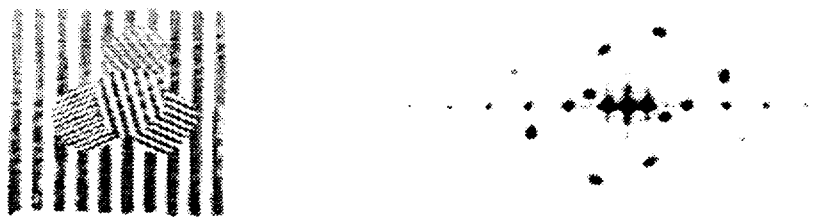


Figure 3.10. Complex texture image consisting of spatial frequencies of 10, 20, 30, 40, and 50 cycles/cm with its Fourier transform

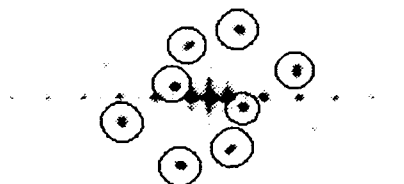


Figure 3.11. Demonstration of fundamental frequency segmentation technique. Circled spectral coefficients corresponding to the fundamental frequencies would be passed and all else blocked.

The images were displayed on the LCTV by connecting the TARGA framegrabber video output cable to the video input plug of the LCTV and switching the LCTV to "line" mode. The FLIR images had previously been translated to TARGA format by John Cline (10:120). No enhancements or preprocessing of any kind were performed on the input FLIR images. The TARGA FLIR files all had a .HLF suffix and had been reduced from an original 240 x 640 pixels to 71 x 320 pixels. Placing them at a specific location on the LCTV required using the user interactive vendor program TESTTARG.EXE which was supplied with the TARGA 8 board when it was purchased. TESTTARG.EXE allows direct access to individual TARGA commands like GETPIC, PUTPIC, LIVE, DIS, ERASE, GRAB, etc. To center the FLIR image on the LCTV, the TARGA command GETPIC was used, and the bottom left-hand corner of the FLIR image was placed at pixel location (100, 200), i.e. (x_c, y_c) , on a 512 x 512 screen. Another vendor program, TRUE_ART.EXE, was also available, and it was mouse-driven. However, it was a canned program and did not allow direct access to the TARGA commands for specific placement of images. Documentation for both programs and descriptions of TARGA commands are included in the TARGA 8 manuals (1, 2). Also, an excellent overview of the TARGA 8 system and a plethora of batch files written for the TARGA 8 system can be found in the Cline thesis (10).

3.4.2.4 Real-time FLIR Imagery on an LCTV Real-time FLIR input imagery was used to test the spatial filters for their ability to segment objects in cluttered background in real time. The imagery was made available through Osvaldo Perez (30) and dubbed onto an LCTV 8 mm VCR tape. It was then played back with the LCTV in the optical setup. No enhancements or preprocessing of any kind were performed on the input FLIR imagery.

3.5 Summary

This chapter presented the theory and methodology behind implementing orientation specific, bandpass spatial filters designed to discriminate texture based on passing dominant spatial frequencies at specific orientations using symmetric aperture pairs. Three major filter designs were described: 1) symmetrically located circular apertures (pinhole pair filters) implemented on heavy, black aluminum foil; 2) sine and cosine Gabor filters implemented with detour-phase computer generated holograms and photoreduced on glass slides; and, 3) pinhole pair filters displayed on an

LCTV for real-time filter selection. Also, the method of testing the spatial filters designed was presented by describing the experimental setup and the design and implementation of the input images.

IV. Results and Discussions

4.1 Introduction

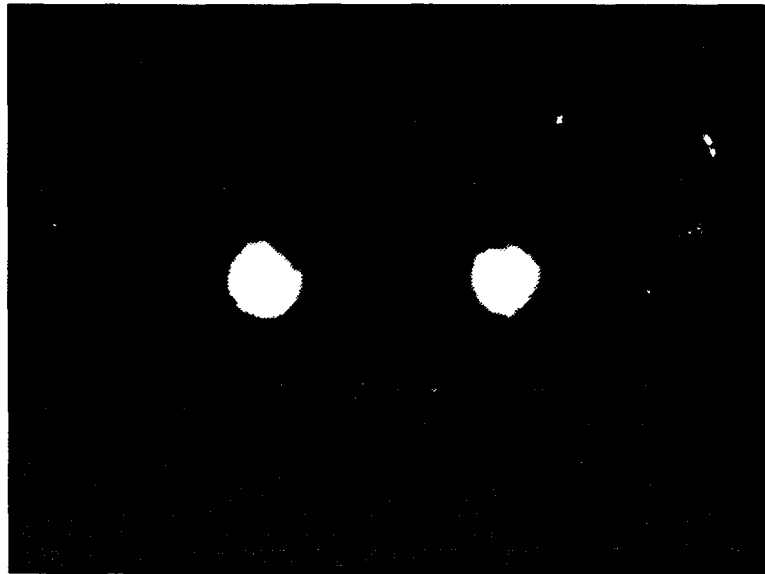
This chapter presents and discusses the results from characterizing and testing the three different implementations of orientation specific, bandpass spatial filters. Characterization was performed as one way of comparing the filter implementations based on their intensity profiles and their associated wavelet patterns. Testing the spatial filters determined how well the different filter implementations could segment the various input images and how well the optical segmentation results compared with the digital segmentation results from the Ayer thesis (3). No preprocessing or post-processing of the input images was done in any way in acquiring these results. Also note that many of the digitized camera images presented were reversed imaged, i.e., light areas are presented dark and dark areas are presented light. This was done to highlight the areas of interest better (and save on toner).

4.2 Characterization of the Spatial Filters

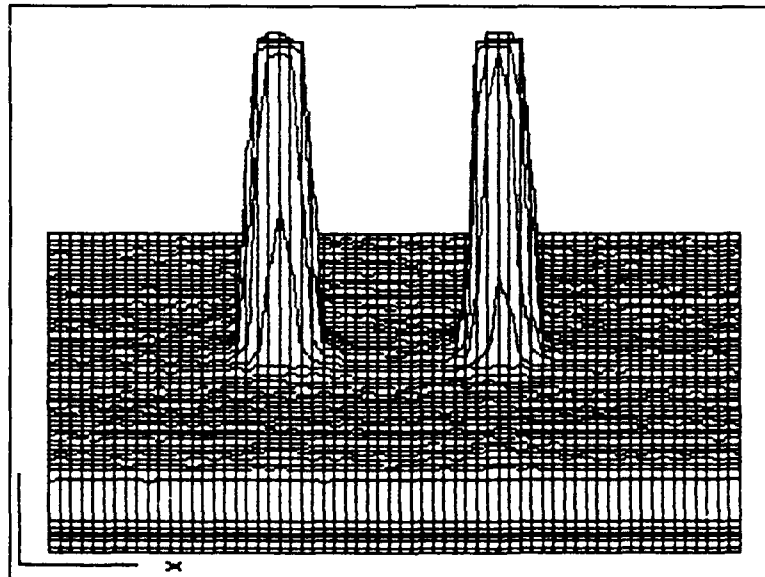
Characterization of the spatial filters was based on three dimensional intensity profiles of the filter images and two dimensional intensity images of the filter spectrums (the wavelet patterns). The 3-D intensity profiles were created on the SPIRICON system using filter images that were originally captured by the Sony CCD camera and TARGA framegrabber combination and then were translated to SPIRICON format using the conversion program TAR2SPIR.EXE written by Cline (10).

4.2.1 3-D Intensity Profiles of Filter Images Figures 4.1, 4.2, 4.3, and 4.4 show the three dimensional intensity profiles of the four different types of orientation specific, bandpass spatial filters that were implemented in this thesis: pinhole pairs on foil, sine and cosine Gabor detour-phase CGHs, and pinhole pairs on an LCTV. Each of the four filters had a pair of symmetrically located apertures with separations and dilations of approximately 2 mm and 1 mm, respectively.

Figure 4.1 shows an image of the pinhole filter on foil and its 3-D intensity profile. Note the sharp cutoff at the edge of the circular aperture which causes the higher order harmonics of the Airy disc pattern in its spectrum shown in Figure 4.6a. Figure 4.2 shows an image of the

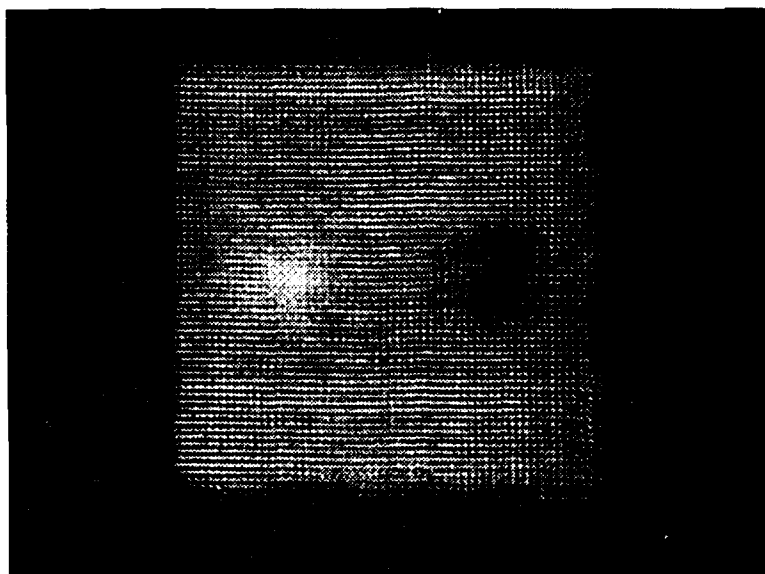


(a)

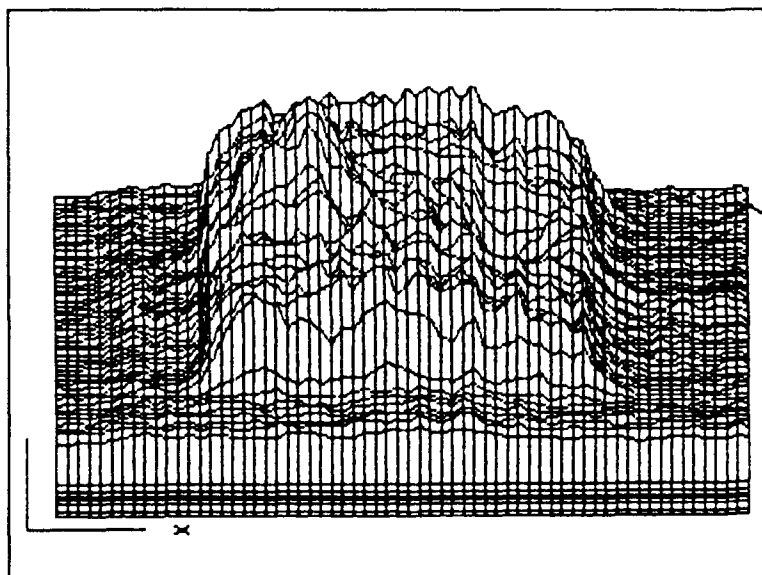


(b)

Figure 4.1. (a) Pinhole pair filter image; (b) Its 3-D intensity profile

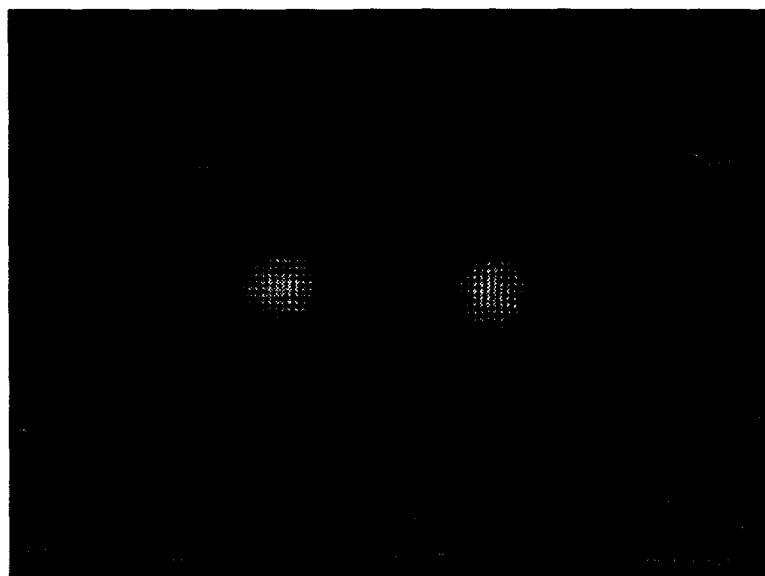


(a)

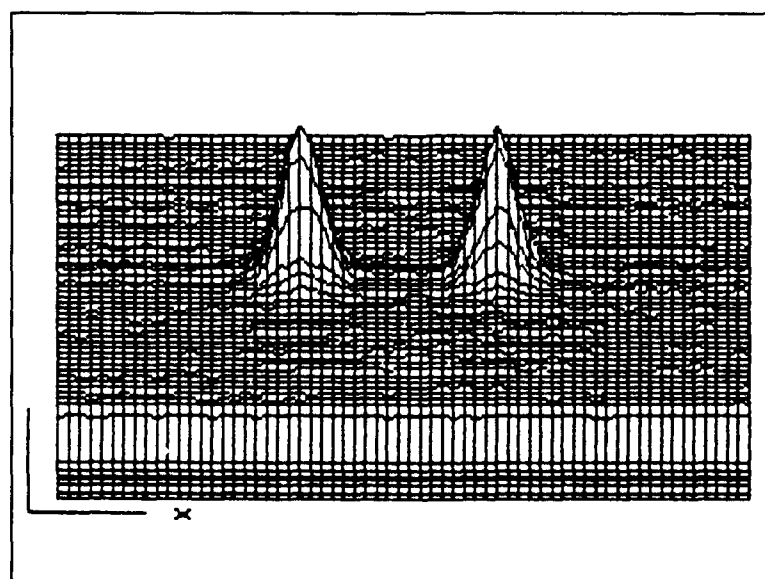


(b)

Figure 4.2. (a) Sine CGH Gabor filter image; (b) Its 3-D intensity profile



(a)

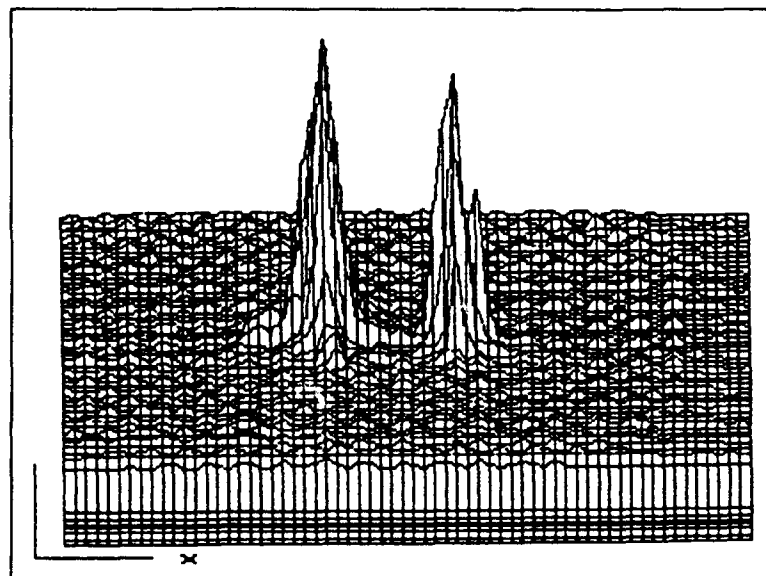


(b)

Figure 4.3. (a) Cosine CGH Gabor filter image; (b) Its 3-D intensity profile



(a)



(b)

Figure 4.4. (a) LCTV Pinhole pair filter; (b) Its 3-D intensity profile

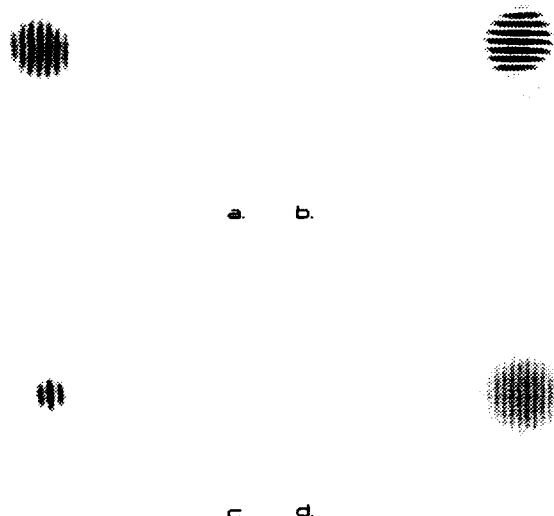


Figure 4.5. Wavelet spectral images of pinhole filters: a. $s=2$ mm $d=.5$ mm, $\alpha=0^\circ$; b. $2,.5,90^\circ$; c. $2,1,0^\circ$; d. $4,.5,0^\circ$

sine Gabor CGH and its 3-D intensity profile. Its 3-D profile appears to be a odd gaussian pair, however, its 2-D Fourier transform did not produce a wavelet. This was probably due to the lack of contrast between the peaks of the image. Thus, no wavelet image is given for the sine CGH in Figure 4.6. Figure 4.3 shows an image of the cosine Gabor CGH and its 3-D intensity profile. Note the smooth gaussian shape of the apertures and the corresponding gaussian shape of its spectrum shown in Figure 4.6b. Apparently, the detour phase CGH technique gives a good approximation of a gaussian. Figure 4.4 shows an image of the LCTV pinhole filter and its 3-D intensity profile. Note the multiple peaks of a single aperture caused by individual pixels. Since pixel separations are approximately $370 \mu\text{m}$, only a few pixels are illuminated for a 1 mm diameter pinhole. Nevertheless, the spectrum of the pair of sampled pinhole images, shown in Figure 4.6c, gives a periodic wavelet.

4.2.2 Filter Spectrums Figure 4.5 shows four different wavelet spectral images from pinhole pair filters in aluminum foil and demonstrates the effect of changing aperture separation,

dilation, and orientation. Notice the rings around the center lobes of the wavelets characteristic of the Airy disc envelope. Essentially, aperture pairs with large dilations produce wavelets which are less localized than aperture pairs with smaller dilations (compare Figure 4.5a with Figure 4.5c). Aperture pairs with wider separations produce wavelets with higher spatial frequencies than aperture pairs with narrower separations (compare Figure 4.5a with Figure 4.5d). The orientation of an aperture pair is perpendicular to the orientation of its corresponding wavelet (see Figures 4.5a and b).

Spectrum 4.5a. was from a pinhole pair filter with a 2 mm separation, .5 mm dilation, and 0° orientation (horizontal). Spectrum 4.5b. was from a pinhole pair filter with a 2 mm separation, .5 mm dilation, and a 90° orientation (vertical). Spectrum 4.5c. was from pinhole pair filter with a 2 mm separation, 1 mm dilation, and 0° orientation. Spectrum 4.5d. was from a pinhole pair filter with a 4 mm separation, .5 mm dilation, and a 0° orientation.

Figure 4.6 compares the three different wavelet spectral images from the three different types of filters implemented. Spectrum 4.6a. came from a pinhole pair filter with a 2 mm separation, 1 mm dilation, and 0° orientation. Spectrum 4.6b. came from a CGH Gabor cosine filter with a 2 mm separation, 1 mm dilation, and a 0° orientation. Spectrum 4.6c. came from an LCTV pinhole pair filter with a 2 mm separation, 1 mm dilation, and a 0° orientation. Comparisons of these wavelet images are discussed in the next section.

4.2.3 Comparison of Spatial Filters A qualitative comparison of the spatial filters was made based on the characterization results given above. Although it appears that the cosine Gabor filter has a gaussian wavelet as its spectrum (a gaussian modulated by a cosine wave), it also contains a DC (center) bright spot (Figure 4.6b). This is an undesirable characteristic, because it means that the filter is passing too much noise (background). The sine Gabor filter could not produce a wavelet probably due to the incorporated DC bias whose intensity overwhelmed any discernible contrast between the positive and negative peaks of the gaussian pairs; hence, it can not segment texture at all. The spectrum of the pinhole filter on foil has no DC term (Figure 4.6a), and its middle lobe appears as localized as the Gabor filter. Moreover, the Airy disc rings of the pinhole pair wavelet are not apparent and do not appear to be a factor at all. The spectrum of the LCTV pinhole filter also has no DC term (Figure 4.6c), however, its periodicity limits its ability

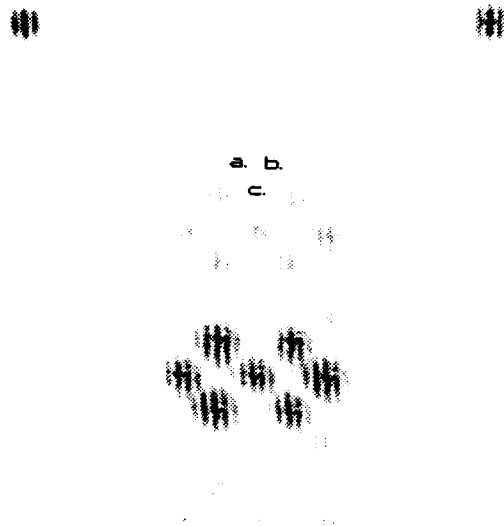


Figure 4.6. Wavelet spectral images of three different filters: a. pinhole wavelet, $s=2$ mm $d=1$ mm, $\alpha=0^\circ$; b. CGH Gabor cosine wavelet, $2, .5, 90^\circ$; c. LCTV pinhole filter, $2, 1, 0^\circ$; d. $4, .5, 0^\circ$

to segment images with large scenes due to the interference between samples. An example of this limitation is shown in testing results with template slides (Figure 4.12). Thus, although none of the filters are optimized, the pinhole filter on foil appears to have the best chance to segment objects out of a cluttered scene, since it can block all of the background noise.

4.3 Testing Results and Discussion

All three major types of filters were tested with input images described in Section 3.4.2. The results of these tests are presented in the following paragraphs. It was found during the testing that the Gabor CGH filters did not segment well, apparently because their backgrounds were not opaque enough to block the bright DC components of the image spectrums. Also, it was found that the LCTV pinhole filters did not perform well because the segmented output was difficult to observe due to interference from the other periodic terms. Hence, most of the results presented

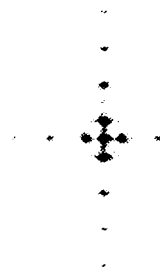


Figure 4.7. Simple texture image of two orientations at 10 cycles/cm, and its Fourier transform

are from segmenting the input images with the pinhole filters on foil.

4.3.1 Testing With Texture Slides Initially, filters with aperture pairs at a 0° orientation and a 2 mm separation were tested with a simple texture image to see if the filters could segment a known image. The simple texture was made up of 10 cycle/cm lines at two perpendicular orientations. It is shown in Figure 4.7 with its Fourier transform. Recall that a separation of 2 mm corresponded to a 10 cycle/cm spatial frequency for the experimental setup described in Chapter III. Hence, the single orientation filters should be able to segment one of the texture orientations and not the other. The results of segmenting the texture slide using a pinhole filter, a cosine Gabor CGH filter, and a sine Gabor CGH filter are shown in Figures 4.8, 4.9, and 4.10, respectively. Figure 4.8 shows complete discrimination of the middle texture from the outer texture. This was due to the ability of the aluminum foil to completely block all of the spectrum except for the part corresponding to the middle texture. The higher frequency of the segmented texture probably resulted from having magnified the spectrum of the texture slide and then filtering the spectrum with apertures whose corresponding spatial frequency was much higher than that of the original texture. Figure 4.9 shows incomplete discrimination of the middle texture. Even though most of the outer texture is blocked, complete segmentation is most desirable. Based on this result, cosine Gabors using detour phase CGHs were not used for segmenting images for the remainder of the research. Figure 4.10 shows no discrimination of the middle texture whatsoever. Based on this result, sine Gabor detour phase CGHs were not used for segmenting images for the remainder of the research. Segmentation results using the simple texture slide and the LCTV filter were very

poor and unrecognizable due to aliasing and are not shown. Thus, investigation of real-time filter selection was not pursued any further in the research.

Next, more complex textures were segmented using the pinhole pair filters to determine how many orientations and spatial frequencies could be segmented at one time. A sample of these results is shown in Figure 4.11. The texture image was made up of a pattern with frequencies of 20, 30, 40, and 50 cycles/cm and a background of 10 cycles/cm. Recall, it is shown with its Fourier transform in Figure 3.10. The pinhole filter consisted of four aperture pairs at separations of 4, 6, 8, and 10 mm corresponding to the 20, 30, 40, and 50 cycles/cm in the pattern. The pinhole pair filters were chosen for segmenting the complex textures because of their ease of implementation. This degree of flexibility was never established with the other two implementations of filters.

4.3.2 Testing With Template Slides The template slides of trucks, tanks, and F-15's are essentially "pre-segmented", since they consist of constant intensity silhouettes with no background clutter. However, they were a good transition to segmenting the FLIR images by helping to calibrate and optimize aperture separations and dilations to objects of similar size. Template slide segmentation was accomplished mainly with pinhole pair filters implemented on the heavy, black aluminum foil. Segmentation results using the other filter designs was not good. In particular, segmentation of a template slide using the LCTV pinhole pair filter was poor due to low resolution of the LCTV. This result is presented in Figure 4.12.

Proper aperture dilation which corresponds to wavelet localization was found to be of utmost importance to obtain highly detailed segmented images. If the aperture dilation was chosen too small, its corresponding wavelet overshadowed any detail in the input image. For example, a first try at segmenting a "small" truck shown in Figure 4.13a was to use a pinhole pair filter with 2 mm separations, .5 mm dilations, and different orientations of 0° , 90° , and a combination of both resulting in the segmentation images shown in Figures 4.13b-d, respectively. Figures 4.13b and c show wavelets correlating on edges in the truck image; however, the wavelets are so large that they overshadow any detail within the segmented image and interfere with one another. Hence, the segmented image that resulted from the combined filter shown in Figure 4.13d had hardly any resemblance to the input image.

The best combination filter for segmenting the small truck template was found to be a



Figure 4.8. Segmentation of a simple texture image using a pinhole filter



Figure 4.9. Segmentation of a simple texture image using a cosine Gabor CGH filter



Figure 4.10. Segmentation of a simple texture image using a sine Gabor CGH filter



Figure 4.11. Segmentation of a complex texture pattern using an pinhole pair filter

pinhole pair filter with 6 mm separations, 3 mm dilations, and orientations of 30, 90, and 150°. The orientations were chosen in order to optimize the space available on the filter. Once the optimal filter was determined, a permanent filter was fabricated by drilling the circular apertures into 1/16 inch aluminum squares. A highly detailed edge segmentation of the small truck template slide was achieved using this filter. This result is shown in Figure 4.14f. Note the fine detail along the edges due to the more localized wavelet produced by the filter. Also note that the back edge of the truck was not segmented. This was due to the filter not having a 0° orientation and illustrates the high degree of sensitivity the filter has to orientation.

The other pictures in Figure 4.14 are for comparison purposes and show less than optimal segmentations of the small truck (Figure 4.14a) using different filter configurations of aperture separation and dilation. Figure 4.14b is the same as Figure 4.13d. It comes from correlating the image with a pinhole pair having 2 mm separations, .5 mm dilations, and orientations of 0 and 90°. Figure 4.14c is from correlating the image with a pinhole pair having 2 mm separations, 1 mm dilations, and orientations of 0 and 90°. Figure 4.14d is from correlating the image with a pinhole pair having 4 mm separations, 2 mm dilations, and orientations of 0 and 90°. Figure 4.14e is from correlating the image with a pinhole pair having 6 mm separations, 1 mm dilations, and orientations of 0, 45, 135, and 90°. Note that the detail in Figure 4.14d is better than that in Figure 4.14e. Hence, it appears that dilation is more important than frequency for achieving highly detailed correlations. However, as the apertures are dilated larger, separations between aperture pairs should be made correspondingly wider in order to maintain modulation within the

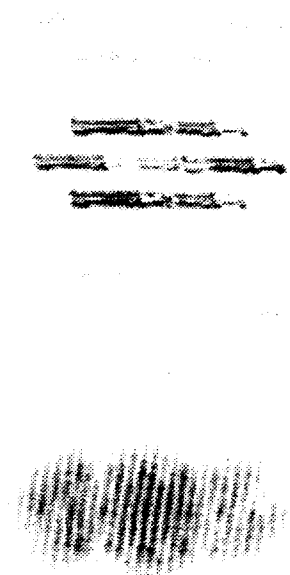


Figure 4.12. Example of segmentation of a "small" truck template slide using a single orientation pinhole pair displayed on an LCTV as a filter. Pinhole separation was 2 mm. Dilation was 1 mm. Orientation was 0° . top: original image with LCTV in filter plane turned off; bottom: segmented image with LCTV displayed pinholes turned on

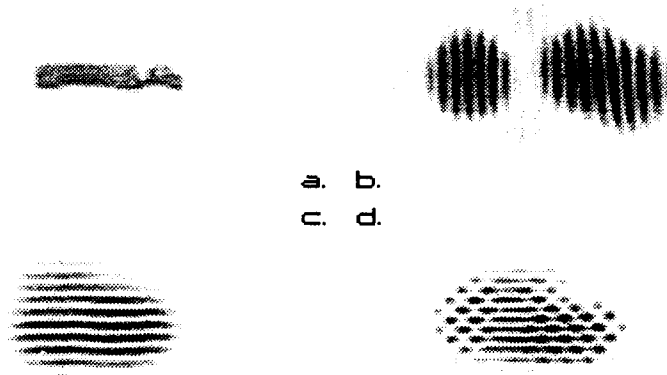


Figure 4.13. Example of a poorly segmented template slide using a pinhole filter with apertures chosen too small. a. image of template slide; b. Segmented image using pinhole filter at 0° orientation; c. Segmented image using pinhole filter at 90° orientation; d. Segmented image using pinhole filter at 0 and 90° orientations

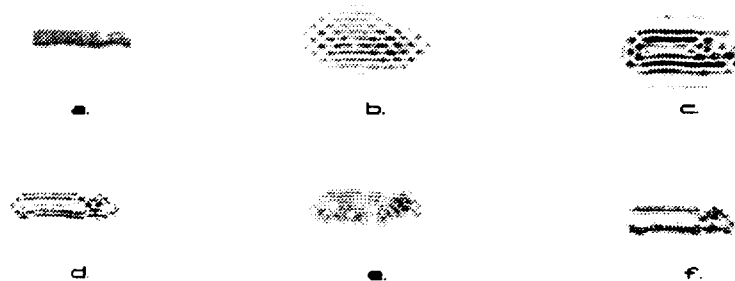


Figure 4.14. Segmentation of a truck template slide using five different pinhole filters. a. image of template slide; b. separations = 2 mm, dilations = .5 mm, orientations = 0 and 90° ; c. $s = 2$ mm, $d = 1$ mm, $o = 0$ and 90° ; d. $s = 4$ mm, $d = 2$ mm, $o = 0$ and 90° ; e. $s = 6$ mm, $d = 2$ mm, $o = 0, 45, 90, \text{ and } 135^\circ$; f. $s = 6$ mm, $d = 3$ mm, $o = 30, 90, \text{ and } 150^\circ$



Figure 4.15. Segmentation of a multiple object template slide using a multiple orientation pinhole filter. a. image of template slide; b. segmented template

more localized wavelet.

As a final example of template segmentation with circular apertures, Figure 4.15 shows a finely detailed segmentation of a multiple object template slide consisting of a truck, a jeep, and two tanks using the 6 mm separation, 3 mm dilation, multiple orientation circular aperture filter described above.

4.3.3 Testing With Static FLIR Images An example of static FLIR segmentation using the FLIR image REFJ16 imaged onto the LCTV and a permanent pinhole filter on an aluminum square with 4 mm aperture separations, 2 mm aperture dilations, and two orientations of 0 and 90° is shown in Figure 4.16.

The segmented images are not as detailed as the ones obtained in the template testing because pinhole separations were limited to 4 mm and pinhole dilations were limited to 2 mm due to the low resolution of the LCTV which is the same filter used for segmentation in Figure 4.14d. In other words, the pinhole dilations could not have been made any wider without passing the higher order periodic spectrums of the LCTV and prevent the segmentation. A graphic example of this is shown in Figure 4.17, where the spectrum of the LCTV is shown with circles drawn on it depicting the pinhole pair locations and the 2 mm pinhole dilations. A second example of static FLIR segmentation using the FLIR image REFM13 imaged onto the LCTV and the identical filter described above is shown in Figure 4.18

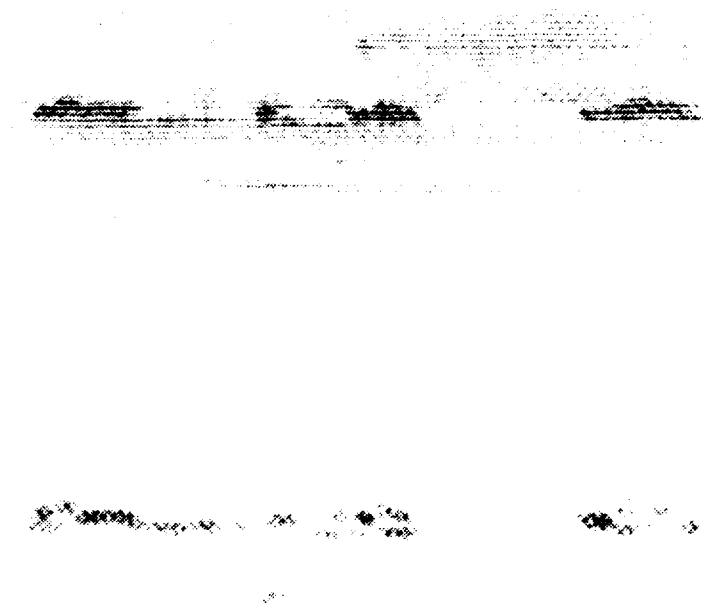


Figure 4.16. Segmentation of static FLIR image REFJ16 using a pinhole filter. top: original FLIR image; bottom: segmented image

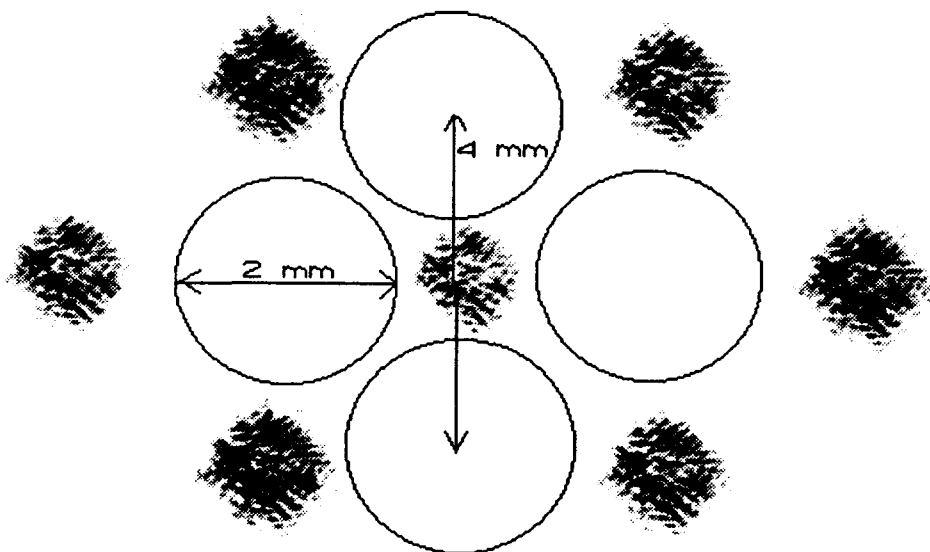


Figure 4.17. Spectrum of Sony Walkman LCTV with circles drawn on top depicting a pinhole filter with 4 mm separations, 2 mm dilations, and 2 orientations

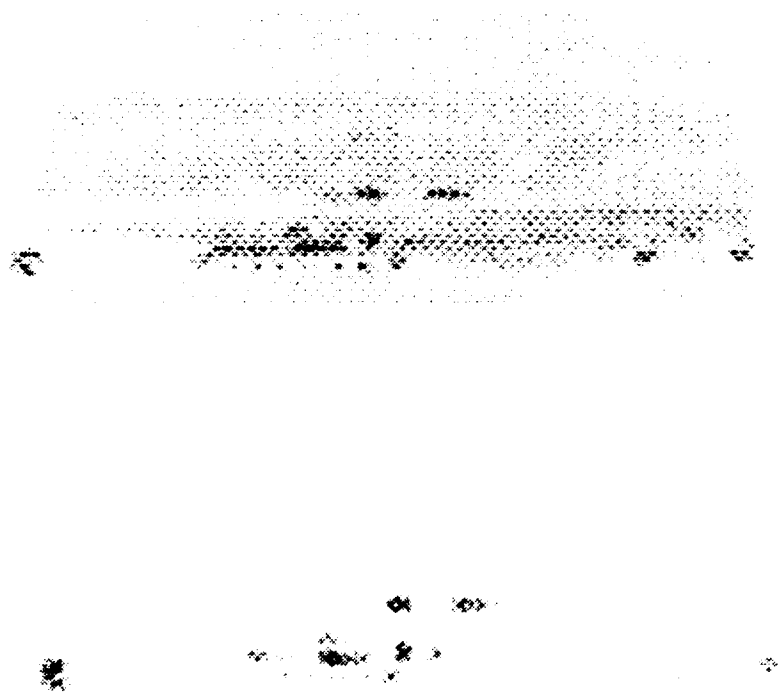


Figure 4.18. Segmentation of static FLIR image REFM13 using a pinhole filter. top: original FLIR image; bottom: segmented image

4.3.4 Testing With Real-Time FLIR Imagery The real-time FLIR imagery was segmented using the same permanent circular aperture filter as was used for static FLIR segmentation. A split-screen video tape was made showing the unsegmented FLIR tape on the upper left-hand corner of the screen and the segmented image on the upper right-hand corner of the screen. Figure 4.19 shows the optical configuration used to observe both the segmented and unsegmented real time FLIR images synchronously, using a beamsplitter placed just before the filter, a second lens, a second CCD camera, and a quad input video processor. The second lens, L_5 , had a focal length of 250 mm, which was smaller than the 300 mm focal length of L_4 . Hence, the unsegmented FLIR image scene is shown slightly smaller than the segmented FLIR image.

In this forum, the real power of optical segmentation can be observed and appreciated, because of its ability to perform instantaneous two-dimensional Fourier transforms. A similar digital segmentation algorithm would be bogged down very quickly trying to calculate Fast Fourier transforms (FFT's) and inverse FFT's at 30 frames/sec. Two digitized frames of the video (not synchronous) are shown in Figure 4.20. Noise around the edges of the circular window was inherent noise from the lenses and the LCTV screen. When seen in real time, these noisy bright spots are constant and don't change (compare noise around edge in segmented FLIR image, frame 1 to noise around edge in segmented FLIR image, frame 2). Further post-processing of the segmented FLIR imagery could be accomplished to remove this constant noise factor.

4.4 Summary

This chapter presented and discussed the characterization and testing of the three types of orientation specific, bandpass spatial filters designed and implemented in this research effort. Pinhole pair filters implemented on heavy, black aluminum foil were demonstrated to have the best segmentation capability out of all three filter designs. When an optimal pinhole filter was found, it was made permanent by drilling circular apertures into aluminum squares. The Gabor CGH filters implemented on holographic glass slides exhibited the expected intensity profiles of odd and even gaussian pairs, but the contrasts of the emulsion on the glass slides could not be made opaque enough to block the unwanted portions of the image spectrum. Pinhole pair filters implemented on the LCTV had poor segmentation capability because of aliasing of the periodic segmented images due to the low resolution of the LCTV. The low resolution of the LCTV was

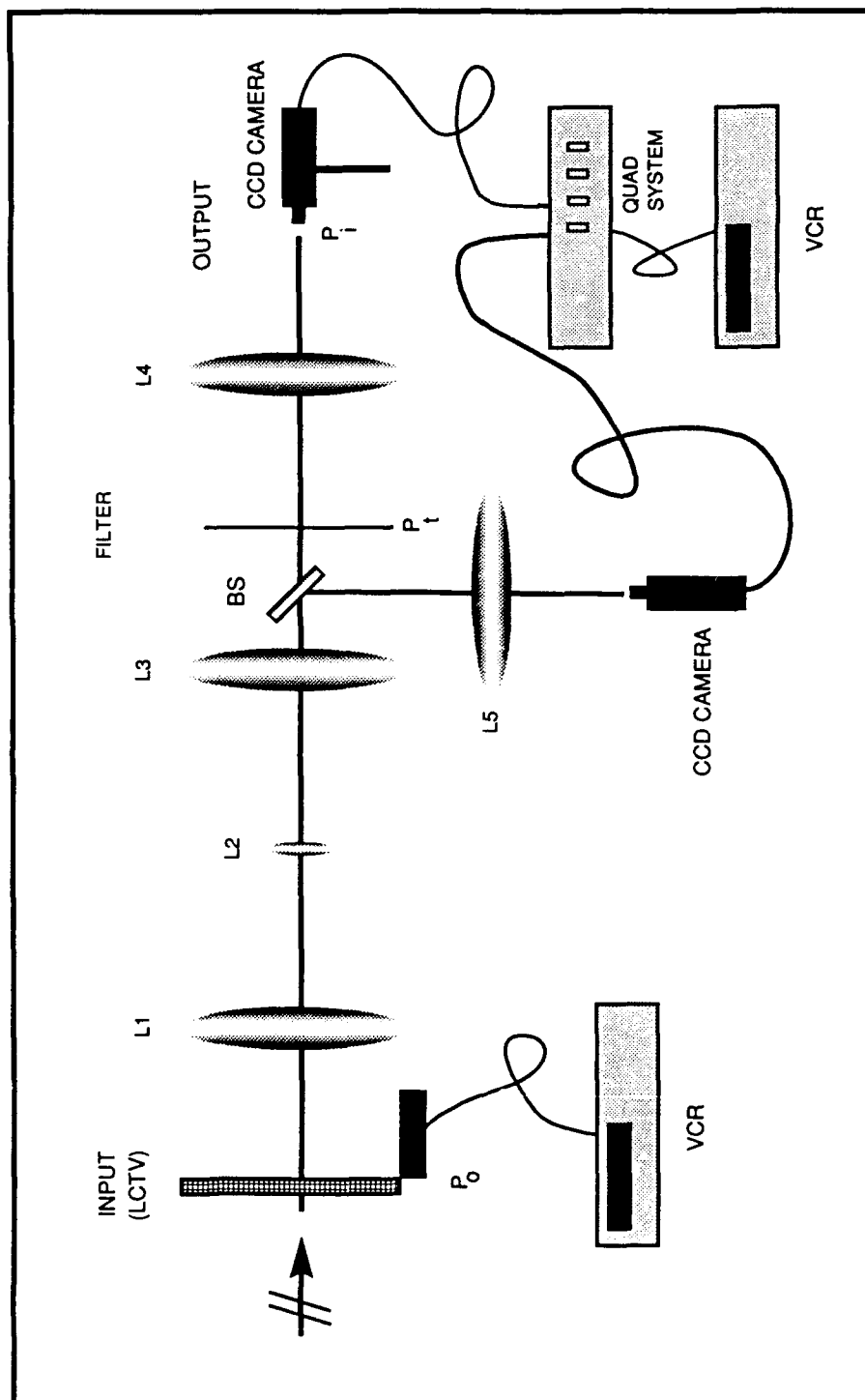


Figure 4.19. Optical setup used for observing segmented and unsegmented real time FLIR images synchronously

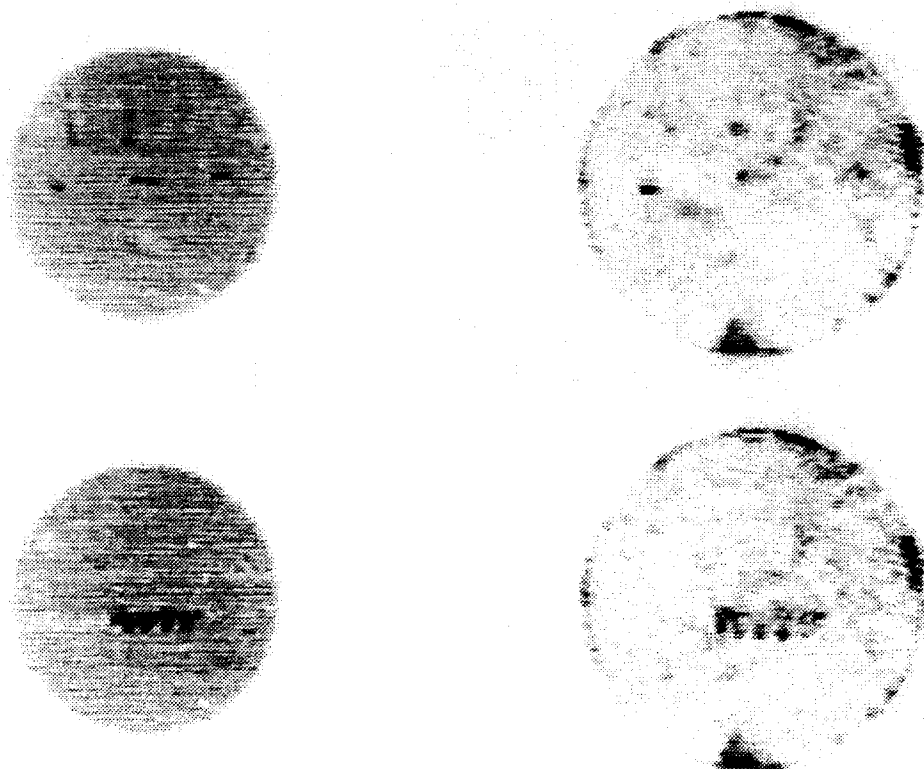


Figure 4.20. Segmentation of two frames of real-time FLIR imagery using a circular aperture pair filter with two orientations, 0 and 90°. top left: original FLIR image, frame 1; top right: segmented FLIR image, frame 1; bottom left: original FLIR image, frame 2; bottom right: segmented FLIR image, frame 2

also a hindrance when used as an input medium for the FLIR images. Segmentation of the FLIR images was not as detailed as it could be because the low resolution of the LCTV limited the separation and dilation of the filter apertures. Real-time optical segmentation of FLIR imagery was demonstrated.

V. Conclusions and Recommendations

This chapter presents a summary of thesis results, provides conclusions based upon these results, and offers recommendations for future research efforts.

5.1 Summary

There were two major goals of this thesis: 1) Design and implement orientation specific, bandpass spatial filters for use in an optical setup including Gabor filters and filters implemented on an LCTV for real-time filter selection; 2) Test these spatial filters for their ability to segment various input images including FLIR imagery displayed on an LCTV.

Three major filter designs were developed. The first design was simple pinhole pair filters implemented on heavy, black aluminum foil. They were modeled as symmetrically located circular apertures which correspond to Airy disc wavelets. Because of their simplicity and flexibility, these filters were used most often in this research effort. Segmentation results using these filters turned out to be very good with capabilities of very fine detail. However, because of the low resolution of the LCTV, aperture dilations and separations could not be optimized for segmenting the FLIR imagery. Optical segmentation of static and real-time FLIR imagery was demonstrated using a simple pinhole pair filter. The second design was sine and cosine Gabor filters implemented using detour-phase computer generated holography. The 3-D plots of the Gabor filters showed them to have the correct characteristics of the odd and even gaussian pairs (FT of Gabor wavelets); however, the spectrum of the Gabor filters (Gabor wavelets) showed undesirable DC terms. Consequently, the Gabor filters designed in this thesis did not demonstrate good segmentation capabilities because they passed too much of the image background. The final filter design was pinhole pair filters implemented on an LCTV to investigate the ability of real-time filter selection. The spectrums of the pinholes pairs implemented in this way produced periodic wavelets; however, the resolution of the LCTV was not high enough to keep the segmented images from interfering with one another.

5.2 Conclusions

An automatic, optically based image segmentation scheme for locating potential targets in a cluttered FLIR image has been implemented successfully. By using the proper choice of aperture pair separation, dilation, and orientation, potential targets in FLIR imagery can be optically segmented using spatial filtering techniques.

The most successful segmentation filter design was the simple pinhole pair filter (circular aperture pairs) implemented on heavy, black aluminum foil. This design proved to be easy to implement, highly flexible, and capable of very fine segmentation detail. Highly detailed edge segmentation of template slides was realized in the described optical setup using simple circular aperture pair filters with 6 mm separations, 3 mm dilations, and orientations of 30, 90, and 150°.

Gabor filters implemented with detour-phase holography and photoreduced onto holographic glass plates were not successful segmentation filters due to the inability of the emulsion to block the unwanted portions of the image spectrum. However, due to the success with the pinhole filters, further pursuit of implementing Gabor filters may not be warranted.

Pinhole filters implemented on an LCTV were not successful segmentation filters in the optical configuration used due to the low resolution of the LCTV. Since grey-scale capability is not necessary for this implementation, the use of a higher resolution, binary SLM may be warranted.

The LCTV was successful as an input image SLM for segmentation of static and real-time FLIR imagery. Because the resolution was low, aperture separations were limited to 4 mm, aperture dilations were limited to 2 mm, and orientations were limited to 0 and 90°. However, because of the need for a grey-scale input medium, a higher resolution, binary SLM was not deemed feasible for this application.

5.3 Recommendations

1) Further investigation into real-time filter selection might benefit by incorporating a higher resolution binary SLM instead of the LCTV used in this research effort. For example, the SEMETEX 128 x 128 iron garnet MOSLM has a resolution approximately five times better than the LCTV (i.e., pixel spacing five times closer together), and since grey-scale is not necessary for

implementing circular aperture pairs, the binary capability would be an advantage by enhancing the contrast.

2) Only single frequency, single dilation, multiple orientation filters were used during this research effort, because multiple frequencies or multiple dilations were found to interfere with one another. Lateral inhibition might be the key to getting around this problem by "running" many different single frequency, single dilation, multiple orientation filters at the same time and "choosing" the best correlation output of one of the filters at any given moment for higher level processing. One way to implement lateral inhibition could be to place many single frequency, single dilation, multiple orientation filters at duplicate Fourier planes containing the spectrum of the input image. The duplicate Fourier planes could be made by using multiple beamsplitters positioned in the area just before the original filter plane. Then, multiple lenses and CCD cameras could be used to observe the correlation planes and feed the outputs into a computer. The computer could then parallel process the multiple outputs and chose a "winning" correlation image at any given moment based on, say, average pixel brightness and pass the pixel coefficients to a higher level of processing.

Appendix A. *Detour Phase Hologram Production*

The following program, `Gabor_Filter`, generates a plotfile that can be used to produce detour phase holograms of Gabor filters on a laser printer. Examples of Gabor filter holograms are shown in Figures 3.5 and 3.6. The program was written in FORTRAN code in order to take advantage of the METALIB library of plotting programs available on the UNIX system at AFIT. It's is a modified version of a program presented in an AFIT thesis by Vicky Robinson (32:37-38) to generate moment holograms.

This Appendix is divided into four sections. First, the program is presented; second, the computational processes and variables of the program are explained; third, some modifications in the Robinson program for compilation purposes are discussed; and last, methods of compiling, previewing, plotting, and photoreducing the holograms are explained.

A.1 *Gabor_Filter Program*

```
      Program GABOR_FILTER
C*****
C      This program generates a plot on the IMAGEN printer that
C      can be used to generate a computer generated hologram of
C      Gabor filters.
C      Written by Chris Veronin, Summer 1990
C      Modified from a CGH program written by Vicki Robinson
C
C*****
      Parameter (D=64.0000)
      character*25 filename
      Integer ntyp, nbeg, nend, norient, nang
      Real D, x, y, hmag, df, rf
C
      Print*, 'Plot filename to be created: '
      Read (5,2000) filename
2000  Format (a10)
      Print*, 'Enter "0" for cosine or "1" for sine Gabor.'
      Read(5,*) ntyp
      Print*, 'Beginning Order? (0,1,2,or 3)'
      Read(5,*) nbeg
      Print*, 'Ending Order? (0,1,2,or 3)'
      Read(5,*) nend
```

```

Print*, 'Number of Orientations? (1,2,3,or 4)'
Read(5,*) norient
Print*, 'Radius Factor? (Default is 2 for octave reln)'
Read(5,*) rf
Print*, 'Dilation Factor? (Default is 2 for octave reln)'
Read(5,*) df
nang = 2 * norient

C
Call Setplot(filename,1,0,.false.)
Call mapxy(0.,1.,0.,1.,0.,1.,0.,1.,0,1)
Do 20 x = 1, D
Do 10 y = 1, D
Call Gabor(D, x, y, ntyp, nbeg, nend, df, rf, nang, hmag)
Call box(x, y, hmag, ntyp)
10 Continue
20 Continue
Call Endplot
End

C
Subroutine Gabor(D, x, y, ntyp, nbeg, nend, df, rf, nang, hmag)
Real D, x, y, x0, y0, gaus, gausx, gausy
Real s, r, theta, Phi, hmag, df, rf
Integer nhalf, nbeg, nend, nang, ntyp
Parameter (PI=3.141592654)
Parameter (theta = (2*PI)/nang)
hmag = 0.00000
Do 40 i=nbeg,nend
Do 30 j=0,(nang-1)
r = (D/(rf**(4-i)))
s = (df**i)
Phi = j*theta
Xterm = r*cos(Phi)
Yterm = r*sin(Phi)
x0 = (D/2) + Xterm
y0 = (D/2) + Yterm
gausx = exp(-(((abs(x-x0))/s)**2))
gausy = exp(-(((abs(y-y0))/s)**2))
gaus = gausx*gausy
nhalf = nang/2
If (ntyp .EQ. 1 .AND. j .GE. nhalf) then
hmag = hmag - gaus
Else
hmag = hmag + gaus
Endif
30 Continue

```

```

40  Continue
    Return
    End
c
Subroutine box(x, y, hmag, ntyp)
  Real x, y, hmag
  Integer ntyp, icx, icy, ih, ilx, ily
  Parameter (iboxw=35, iw=17, ihmax=35, iosx=500, iosy=90)
  icx = x*iboxw - (iboxw/2) + iosx
  icy = y*iboxw - (iboxw/2) + iosy
  If (ntyp .EQ. 1) then
    ih = (ihmax/2) + (ihmax/2)*hmag
  Else
    ih = ihmax * hmag
  Endif
  ilx = icx - (iw/2)
  ily = icy - (ih/2)
  Do 50 i = ilx, ilx+iw
    Call drv(i, ily, i, ily+ih)
50  Continue
    Return
    End

```

A.2 Process and Variable Explanation

Essentially, the main program generates the plotfile in three steps. First, it establishes the plotting directions to the printer by calling the METALIB subroutines *Setplot* and *mapxy*. Second, it calls the subroutine *Gabor* to compute the height, *hmag*, of the rectangles in the hologram, one at a time. Finally, after each height is computed, it calls the subroutine *box* which directs the plotting of the rectangle using the METALIB subroutine *drv*. The finished plot is the negative of the desired filter image, because the photoreduction process reverses the contrasts.

A detailed explanation of the function *Gabor* is presented in the next section. Detailed explanations of the METALIB subroutines can be found in either the METALIB manual (online on the UNIX system) or the Robinson thesis, and a detailed explanation of the subroutine *box* can be found in the Robinson thesis (32:38-41).

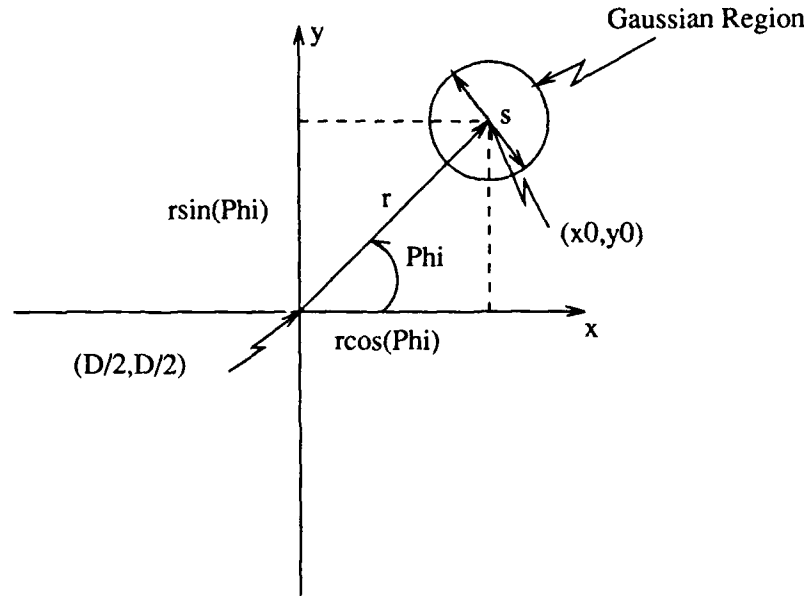


Figure A.1. Location of gaussian regions in Gabor filter holograms

A.2.1 The Subroutine Gabor The subroutine *Gabor* computes the height of any given rectangle in the hologram at location (x, y) . The height is calculated from the following equation:

$$gaus = \exp[-(|x - x_0|/s)^2] \exp[-(|y - y_0|/s)^2] \quad (A.1)$$

where x and y indicate the location of the rectangle in the array $D \times D$, x_0 and y_0 indicate the location of a gaussian region in relation to the center point of the array at $(D/2, D/2)$, and s indicates the dilation of the gaussian regions.

Figure A.1 shows the radius of the frequency rings as r and the angle from the x axis as Φ . The radius r can vary depending on the range of frequency rings input (nbeg to nend) and the radius factor, rf . If rf is chosen to be 2, then the program varies the radius r in octave steps, i.e., $D/16, D/8, D/4, \dots, D/[2^{(4-i)}]$. The angle Φ is determined by spacing the gaussian pairs (# of orientations) evenly around the center point relative to the first pair at 0 and π radians. The dilation s is a constant within a frequency ring and varies according to the dilation factor, df , and the range of the frequency rings input. If df is chosen to be 2, then s takes on values of 1, 2, 4, ..., 2^i . s is related to the standard deviation of a gaussian by $\sigma = s/\sqrt{2\pi}$.

If the location (x, y) of the rectangle being calculated is within any gaussian regions, the variable *gaus* will be assigned a non-zero value. Since none of the gaussian regions overlap, the values of the variable *gaus* for each region can be added together for each of the rectangle locations without any problem.

Also, the program makes a distinction between sine and cosine Gabor filters. The "flag" *ntyp* is used to tell the program whether a cosine Gabor filter (*ntyp* = 0) or a sine Gabor filter (*ntyp* = 1) is desired. If *ntyp* is 0, then the program computes only positive gaussian functions and can use the full range of height available for computing gaussian shapes (35 levels). If *ntyp* is 1, then the program incorporates a DC bias at level "17", inverts the height of the second gaussian in the pair, and only has the half range of height available for computing gaussian shapes (17 levels).

A.2.2 Program Operation The program prompts the user for the plot filename (filename), cosine or sine preference (*ntyp*), lowest ring order (*nbeg*), highest ring order (*nend*), number of orientation pairs (*norient*), radius factor (*rf*), and the dilation factor (*df*). It was originally written with octave relationships in mind and later was modified for more flexibility, so there was a method to my madness. All the parameters are self explanatory except for the radius and dilation factors. To determine these, the dimensions of the reduced filter must be decided upon.

Let's say we desired a single ring cosine filter with 2 mm aperture separations and 1 mm aperture dilations after a 50x photoreduction of the output transparency. Set *ntyp* = 0, *nbeg* = *nend* = 2, and *norient* = 1 or 2. Now, the radius of the apertures from the center point on the hologram is based on $D/(rf^2)$. Since each of the celis is approximately 2.94 mm wide, and we want a radius of 50 mm ($50 \text{ mm}/50 = 1 \text{ mm}$), then we want $D/(rf^2) = 17$. And since $D = 64$, we should set $rf = 1.94$. Next, the aperture dilation is based on the radius of the aperture df^2 . Thus, since we want a aperture radius of 25 mm ($25 \text{ mm}/50 = .5 \text{ mm}$), then we want $df^2 = 8.5$, or $df = 2.92$.

A.3 *Compiling, Previewing, Plotting, and Photoreducing*

A.3.1 *Compiling* To compile the program on the UNIX system at AFIT the following command should be used:

```
f77 -o programname programname.f -lmetalib (A.2)
```

Then, by typing the *programname*, the plotfile can be generated. Note: Metalib is a library residing in the UNIX mainframes at AFIT (it does not need to be in your path). Metalib is not on all the UNIX systems, but as of Summer 1990 it was at least on Blackbird and Galaxy.

A.3.2 *Previewing* Before plotting the hologram on the laser printer, it's a good idea to preview it first on the computer screen. Especially, since the holograms take an average of 20 minutes plotting time each on the IMAGEN printer.

The plots can be previewed on the terminal by using a Tektronix 4012/4014 screen emulator and the following command:

```
plot pltname -Ttek (A.3)
```

Two Tektronix screen emulators were found to work well. One can be found on the SUN Workstations by using the command *Tektool*. The other can be found on the MicroVax system by opening a Tektronix 4012/4014 window. Clear the screen before previewing with the *clear* command. Also, make sure the system environment is set for the right terminal by using the *set term = tek* command.

An alternative method is to print the hologram to a file using the postscript printing command (see next section on plotting), and then use a postscript previewer to examine the hologram. For example, the NeXT machines in room 2011, Bldg 642, have postscript previewers that have been used for this purpose.

A.3.3 *Plotting* To make a hologram, a transparency should be used as the plotting medium. The hologram can be plotted on an IMAGEN printer by using the *mit* command:

```
mit pltname |lpr -P(printername) (A.4)
```

or it can be plotted on a Postscript printer by using the *mps* command:

$$mps \ pltname \ |lpr \ -P(printername) \quad (A.5)$$

For postscript previewing purposes, print the hologram to a file using the command:

$$mps \ pltname \ > \ pltname.eps \quad (A.5)$$

An alternative method to printing directly onto a transparency is to print the hologram on white paper using the commands above, and then thermofax the image onto a transparency. The advantage of this method is a darker, more uniform, and higher contrast transparency hologram.

A.3.4 Photoreducing After plotting, the transparency should be photoreduced in order to use it in an optical imaging system. The transparencies generated in this research effort were reduced 50x onto a 2 x 2 x .06in. glass holographic plate. This was accomplished by using a 35 mm lens in the Dekacon optical photoreduction system located in the Cooperative Electronics Materials Processes Laboratory (room 1065) in building 125. Photoreduction procedures can be found in the Robinson thesis (32:42-43), the Childress and Waldron thesis (9:100-103), or in the Dekacon instruction sheets found in a 3-ring binder located with the Dekacon system.

Appendix B. *LCTV Modifications and Limitations*

B.1 Introduction

This Appendix was written to discuss some of the details regarding the modifications, liquid crystal display (LCD) configuration, and resolution limitations of the liquid crystal television (LCTV) used in the optical setup as an amplitude spatial light modulator (SLM).

Over the past five years, LCTVs have been demonstrated as capable amplitude and phase SLMs in optical image processing setups in various research projects (4, 7, 8, 14, 17, 19, 18, 20, 27, 22, 24, 25, 29, 36, 39, 40). The main advantage of LCTVs is low cost (approximately \$100 to \$1200), and their main disadvantage is low resolution (pixel sizes on the order of $370\ \mu\text{m}$). Many researchers have overlooked the low resolution disadvantage in order to implement a low-cost demonstration of dynamic optical image processing.

The main reason for using an LCTV in this research effort was the need for a low-cost, gray-scale SLM in order to demonstrate real-time segmentation of input gray-scale FLIR imagery. The LCTV chosen was a Sony Video Walkman LCTV. The television unit came equipped with a built in 8mm video cassette recorder (VCR), video and audio input/output jacks, a battery pack for portability, and a lot of other nice bells and whistles. It retails for about \$1200. Specifications for the LCD are given in Table B.1. These parameters were taken from a design and specification manual for the Sharp LCD, Reference (35). Two Sony Video Walkman LCTVs and a Sony CCD camera were purchased for this research effort through the thesis sponsor WRDC/AARI-2, POC: Capt Kevin Ayer.

B.2 LCTV Theory

An excellent presentation of theory behind the operation of an LCTV as an amplitude SLM for use in a coherent imaging setup can be found in Reference (23). In addition to theory, this paper characterizes and compares the capabilities of three different LCTVs and discusses the advantages of an active matrix using a thin-film transistor (TFT) at every pixel. Also, Ken Hughes' thesis (18) includes a section on LCTV theory and operation as an amplitude SLM, as well as many of the other references given at the beginning of this Appendix. For a good presentation on the theory and operation of an LCTV used as a phase SLM, see Reference (25).

Table B.1. Mechanical Specifications of Liquid Crystal Display

Parameter	Specifications	Unit
Manufacturer	Sharp	
Model #	LQ424A01	
Addressing method	TFT	
Display format	479 (W) × 234 (H)	Pixels
Active area	81.9 (W) × 61.8 (H)	mm
Screen size (Diagonal)	4	Inch
Pixel pitch	0.171 (W) × 0.264 (H)	mm
Pixel configuration	RGB delta configuration	
Outline dimensions*	110.2 (W) × 85.8 (H) × 20.7 (D)	mm
Weight	170±10	g

* Excluding protrusions

B.3 Modifications

As much as I hated to do it, the Sony Video Walkman had to be modified before it could be used in the optical setup. Essentially, the LCD had to be removed from its hinged case where the backlighting florescent tubes and diffuser resided as well as many of the video and audio electronics. Quite honestly, taking the LCTV apart and removing the LCD was a trial and error exercise, since there was no technical manual available dealing with this kind of "repair". However, the modification was successful. Hopefully the following description of steps taken to remove the LCD from its case will help anyone wishing to modify the second LCTV or wishing to put the modified LCTV back together.

B.3.1 LCTV Disassembly 1) Remove two top screws from back of hinged unit and two bottom side screws from hinged unit (all four have arrows pointing to them) using a jewelers screwdriver. Notice the two side screws are shorter than the top screws.

2) Remove circuit board unit by removing two medium sized upper left and lower right screws and two upper left ribbon cables (ribbon cables slide out after snapping open holders).

3) Remove florescent tubes. Note: blue and red dots were up and on the side of the LCTV with the video/audio jacks; metal contact strips were down.

4) Remove diffuser unit by removing the four corner screws on the unit (long and finely

threaded). Also, need to remove side push-button panel used for setting the clock, etc. by disconnecting its cable from the circuit board unit and removing the two mounting screws.

5) Diffuser unit and upper push-button panel should come out easily exposing the LCD unit. **BE CAREFUL NOT TO SCRATCH THE LCD!** Place a soft cloth under the LCD unit when laying it down.

6) Remove LCD unit from front holder and disconnect its ribbon cable from the circuit board unit.

7) Remove SECOND diffuser plate within LCD unit by first removing the two corner screws (silver) from back of unit and prying metal casings apart at the corners (some finesse will be needed here).

8) After prying apart the metal casings so that diffuser plate is accessible, place the LCD unit so the ribbon cable is oriented up and diffuser plate is exposed.

9) Carefully remove diffuser plate (it's just sitting in there).

B.3.2 LCTV Assembly 1) Put LCD unit back together without diffuser plate installed. Top metal casing goes to outside.

2) Replace small silver screws back in their opposite corners and reconnect LCD unit ribbon cable to circuit board unit.

3) Place a cloth around LCD unit and lay it on top of VCR unit (top of LCTV).

4) Reassemble the hinged unit in reverse order without installing LCD unit, florescent tubes, or side push-button panel.

B.4 LCD Configuration and Spatial Resolution Limitations

The following two subsections detail the LCD pixel configuration and spatial resolution limitations of the Sony Video Walkman LCTV. This research was accomplished in order to figure out the origins of the LCTV spectrum, characterize the LCTV for comparison to other SLMs, and determine the resolution limitations of the LCD.

B.4.1 LCD Configuration The LCD consists of a 2-D array of red, green, and blue (RGB) pixels arranged in a "delta" configuration. Looking under a microscope, the pixels were seen to be in the arrangement shown in Figure B.1. Each of the 234 rows is staggered back and forth and

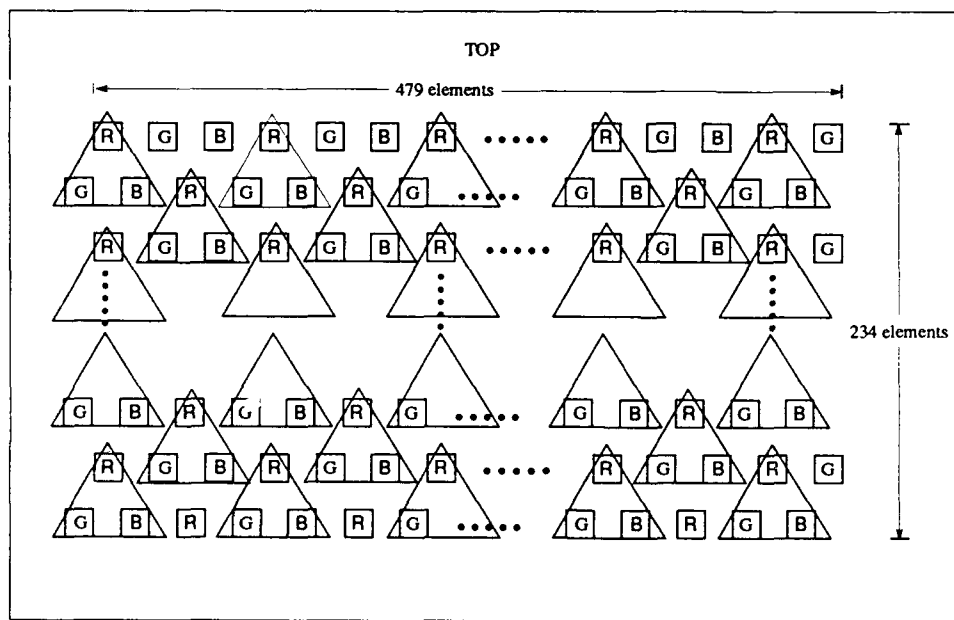


Figure B.1. Sketch of magnified view of RGB pixel arrangement on the LCD. R-red; G-green; B-blue

contain 479 RGB elements. The triangles drawn represent a set of RGB elements that work in unison to form a "composite" pixel. The composite pixels are arranged in a "diamond" pattern, which is analogous to rotating a square mesh by 45°. IT IS THESE COMPOSITE PIXELS AND THEIR SEPARATIONS THAT TRULY ESTABLISH THE RESOLUTION OF THE LCD. Thus, the true pixel array of the LCD can be determined by counting the number of composite pixels along the rows and columns, being careful not to count the same pixel twice. If we count the composite pixels along the top (horizontally), not counting the last two red-green elements, we get 2 composite pixels for every 3 RGB elements. Thus,

$$\frac{2}{3}(479 - 2) = 318 + 1 \text{ (from last red element)} = 319 \text{ composite pixels} \quad (\text{B.1})$$

And along the side (vertically), we get 1 composite pixel for every 2 RGB elements. Thus,

$$\frac{1}{2}(234) = 117 \text{ composite pixels} \quad (\text{B.2})$$

Using these numbers, we see that the LCD has a smaller composite pixel array of approximately 319 (W) \times 117 (H) than what appeared to be presented in the specifications in Table B.1 of 479 (W) \times 234 (H).

Next, composite pixel spacing was calculated using the active area dimensions given in Table B.1 and taking into account the fact that the rows are staggered, we get a horizontal composite pixel spacing of

$$\frac{81.9 \text{ mm}}{319} = .257 \text{ mm} \quad (\text{B.3})$$

and a vertical composite pixel spacing of

$$\frac{61.8 \text{ mm}}{233} = .265 \text{ mm} \quad (\text{B.4})$$

However, because the rows are staggered, the actual composite pixel spacing is determined by finding the hypotenuse of the horizontal and vertical components of the composite pixels, see Figure B.2. Thus, the actual composite pixel spacing was found to be

$$.265^2 + .257^2 = x^2 \quad \text{thus, } x = .370 \text{ mm} \quad (\text{B.5})$$

The composite pixel spacing of .370 mm is equivalent to the pixel spacing of black and white LVTVs (23); however, the contrast of the Sharp LCD is much better due to the TFT active matrix.

B.4.2 Spatial Resolution Limitations The resolution limitations of the LCTV can be best demonstrated by observing its spectrum and determining the range of spatial frequencies that it can resolve before aliasing occurs. The spectrum of the LCTV was observed using the optical setup shown in Figure B.3. L1 was a 250 mm lens which was used to take the Fourier transform of the LCTV image. L2 was a 40x microscope objective which was used to magnify the LCTV spectrum onto the CCD camera. The spectrum of the LCTV with no input image displayed is shown in Figure B.4.

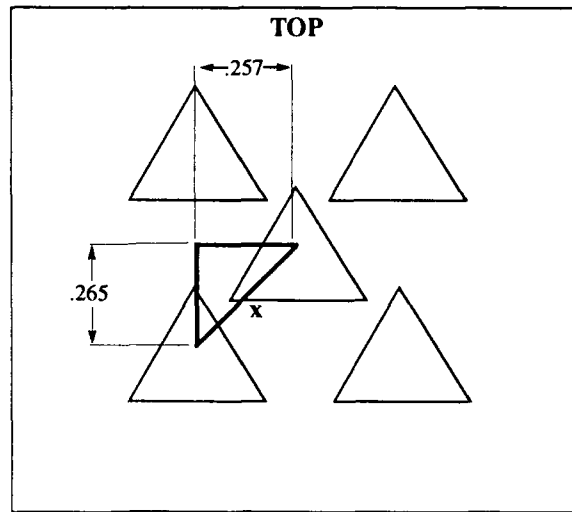


Figure B.2. Sketch showing composite pixel spacing components

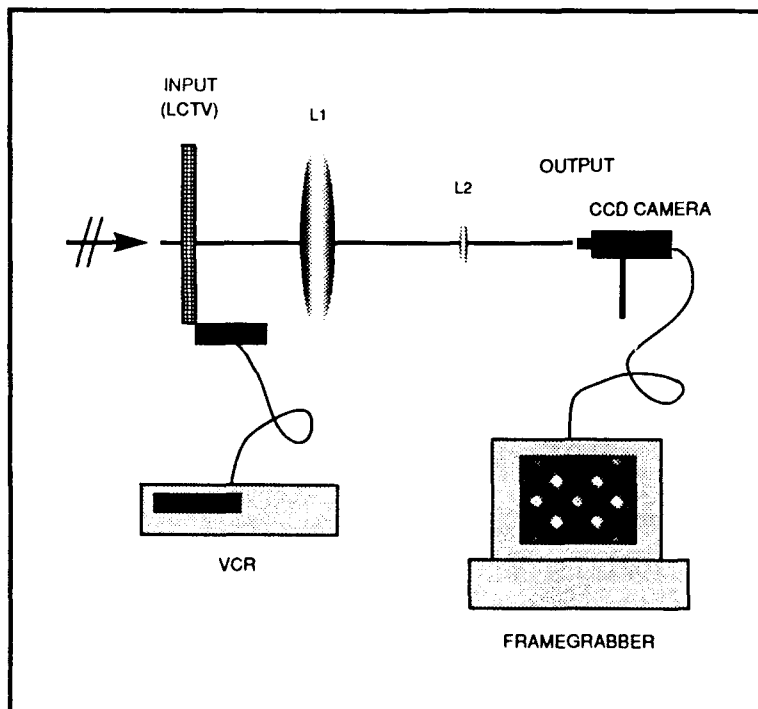


Figure B.3. Optical setup used to observe LCTV spectrum

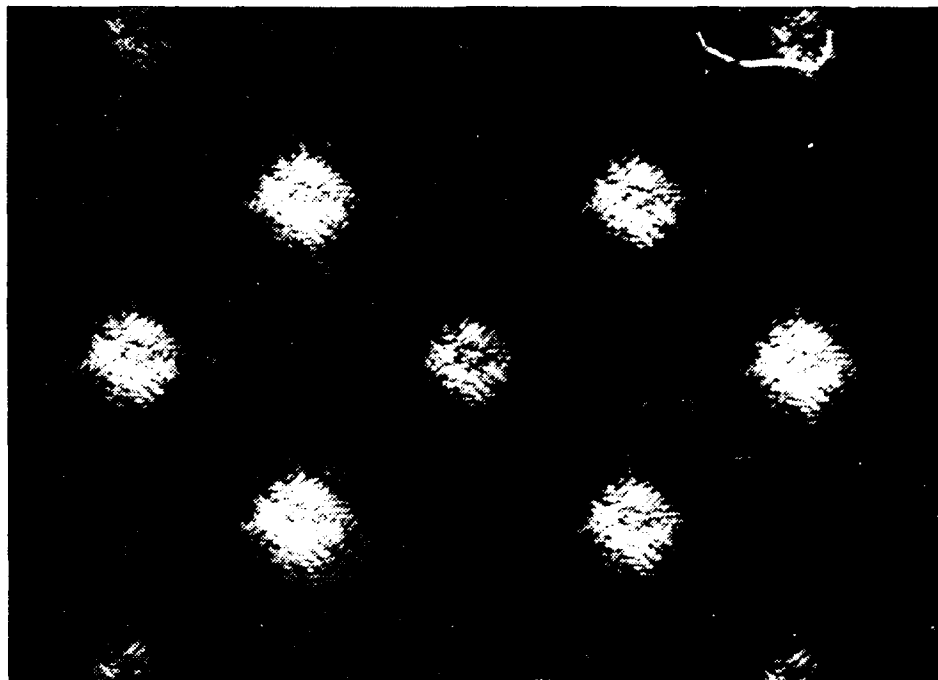


Figure B.4. Spectrum of LCTV with no input image displayed

Bar patterns containing different spatial frequencies were imaged onto the LCTV screen using a Panasonic video camera. It was found that the LCTV can resolve the spectral coefficients from displayed bar patterns containing spatial frequencies of 4 cycles/cm to 12 cycles/cm. Spectral coefficients from spatial frequencies any lower than 4 cycles/cm were lost in the pixel DC, see Figure B.5. Spectral coefficients from spatial frequencies any higher than 12 cycles/cm began to interfere with one another due to aliasing, see Figure B.6. Thus, the resolution of the LCTV is limited to 4 to 12 cycles/cm. No matter how much more the spectrum is magnified, this resolution limitation will remain fixed.



Figure B.5. Spectrum of LCTV with spectral coefficients from 4 cycle/cm bar pattern displayed showing lower resolution limit of LCTV.

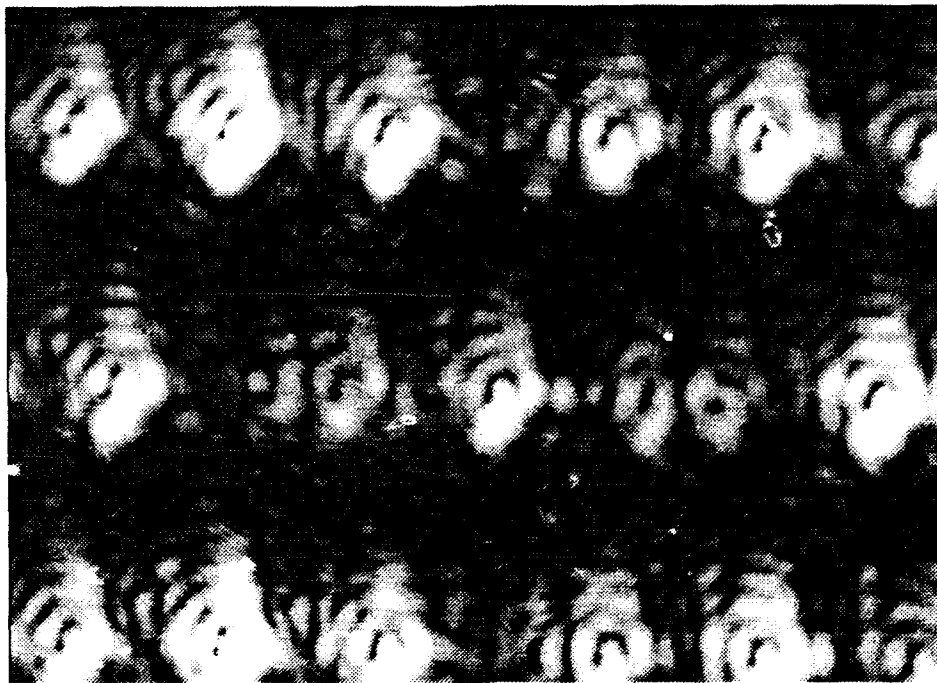


Figure B.6. Spectrum of LCTV with spectral coefficients from 12 cycle/cm bar pattern displayed showing upper resolution limit of LCTV.

Appendix C. Barplot Generation

The following program, Barplot, generates a plotfile that was used to produce barplots of varying frequencies that were, in turn, used to create texture input slides for the spatial filtering experiments described in this thesis. The finished texture slides used are shown in Appendix D. The program was written in FORTRAN code in order to take advantage of the METALIB library of plotting programs available on the UNIX system at AFIT. It uses a modified version of the subroutine *box* written in a program presented in an AFIT thesis by Vicky Robinson (32:37-38) to generate moment holograms.

This Appendix is divided into three sections. First, the program is presented; second, the computational processes and variables of the program are explained; and last, methods of compiling, previewing, plotting, and photoreducing the holograms are explained.

C.1 Barplot Program

```
      Program BARPLOT
C*****
C
C      Program for plotting textured images
C      Written by Chris Veronin
C
C*****
      character*25  filename
      integer      cycles

      write (6,1000) "Plot filename to be created:  "
1000 format (a31)
      read (5,2000) filename
2000 format (a10)
      write (6,3000) "Number of cycles/cm:  "
3000 format (a23)
      read (5,4000) cycles
4000 format (i4)

      Call Setplot(filename,1,0,.false.)
      Call mapxy(0.,1.,0.,1.,0.,1.,0.,1.,0,1)
      Do 30 m = 1, cycles
      Do 20 n = 1, cycles
      hmag = 1.0
```

```

    Call box(cycles,m,n,hmag)
20  Continue
30  Continue
    Call Endplot
    Stop
    End
c
    Subroutine box(cycles,m,n,hmag)
    integer cycles
    iboxw = (2560 - 25)/cycles
    ihmax = iboxw
    iw = iboxw/2
    iosx = ((3328 - (cycles * iboxw)) + 30)/2
    iosy = ((2560 - (cycles * ihmax)) + 25)/2
    icx = m*iboxw - (iboxw/2) + iosx
    icy = n*iboxw - (iboxw/2) + iosy
    ih = ihmax * hmag
    ilx = icx - (iw/2)
    ily = icy - (ih/2)
    Do 10 i = ilx,ilx + iw
    Call drv(i,ily,i,ily+ih)
10  Continue
    Return
    End

```

C.2 Explanation of Program

The program is basically a very scaled-down version of the Gabor_Filter program presented in Appendix A, i.e., make use of what you've got. However, instead of computing the different heights of the cell rectangles, this program sets all the heights to 1.0 and divides the widths of the rectangles into equal values depending on the number of cycles entered at the program prompt. The subroutine *box* is modified slightly in order to take full advantage of the pixel dimensions for an entire sheet of paper for the IMAGEN printer (3328×2560 instead of 3270×2445 as cited in the Robinson thesis). Detailed explanations of the METALIB subroutines can be found in either the METALIB manual (online on the UNIX system) or the Robinson thesis, and a more detailed explanation of the subroutine *box* and its parameters can be found in the Robinson thesis (32:38-41).

C.3 Output Procedures

The previewing, plotting, and photoreduction procedures are the same here as they were for the Gabor CGHs. One difference is that the texture slides shown in Appendix D could not be made directly from these barplots; they had to be cut-out and pasted together, and then transferred to transparencies and photoreduced. The transparencies were photoreduced 20x using the 3in. Wray lens. This produced glass slides with images approximately 1 cm square. Hence, a 10 cycle/sheet transparency reduced 20x would produce a 10 cycle/cm input texture slide.

Appendix D. *Texture Plots*

This Appendix presents four different texture slides made using the barplot program described in Appendix C and a little extra “cut and paste”.

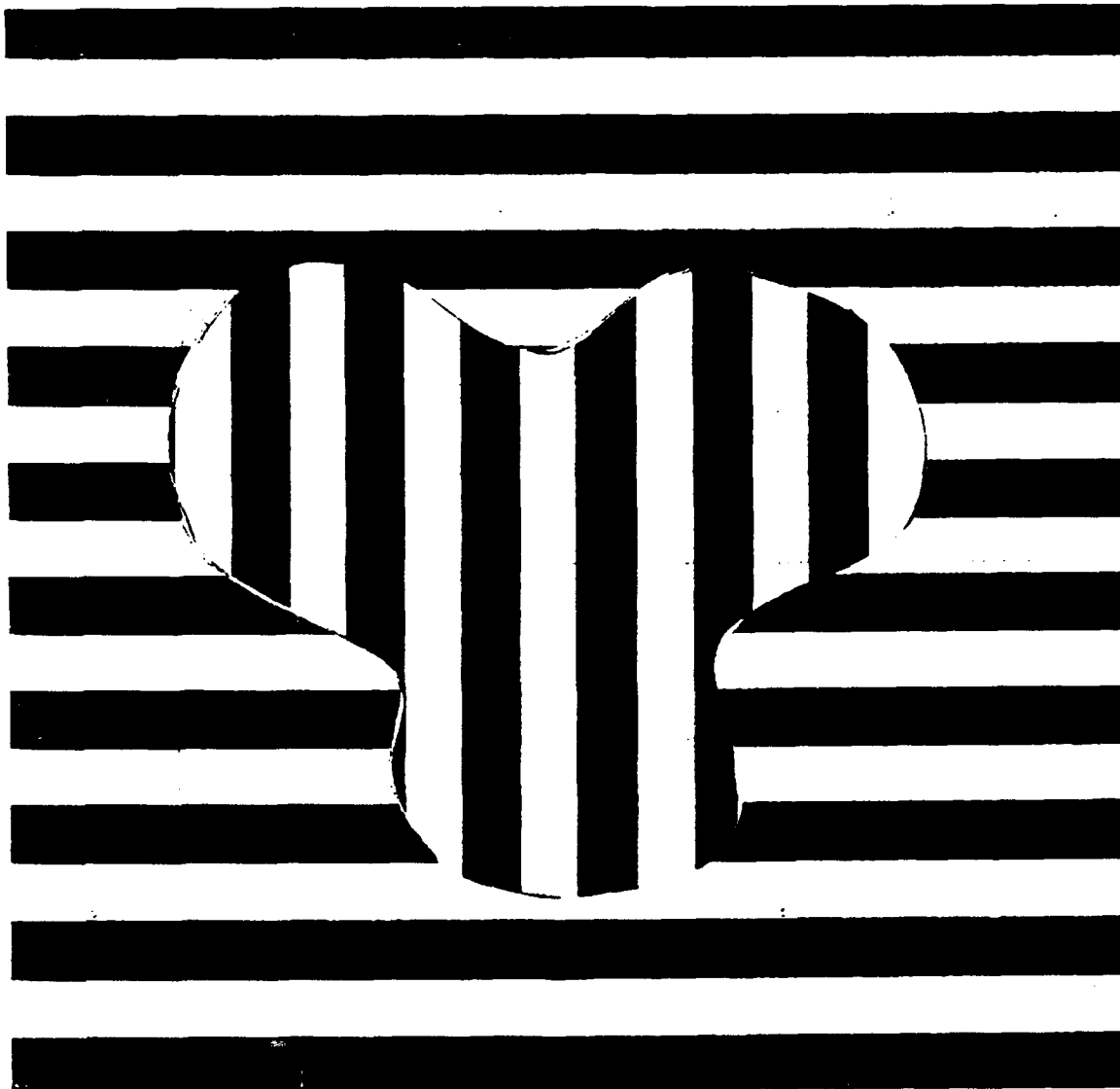


Figure D.1. Example of a simple texture slide with 10 cycles at two perpendicular orientations

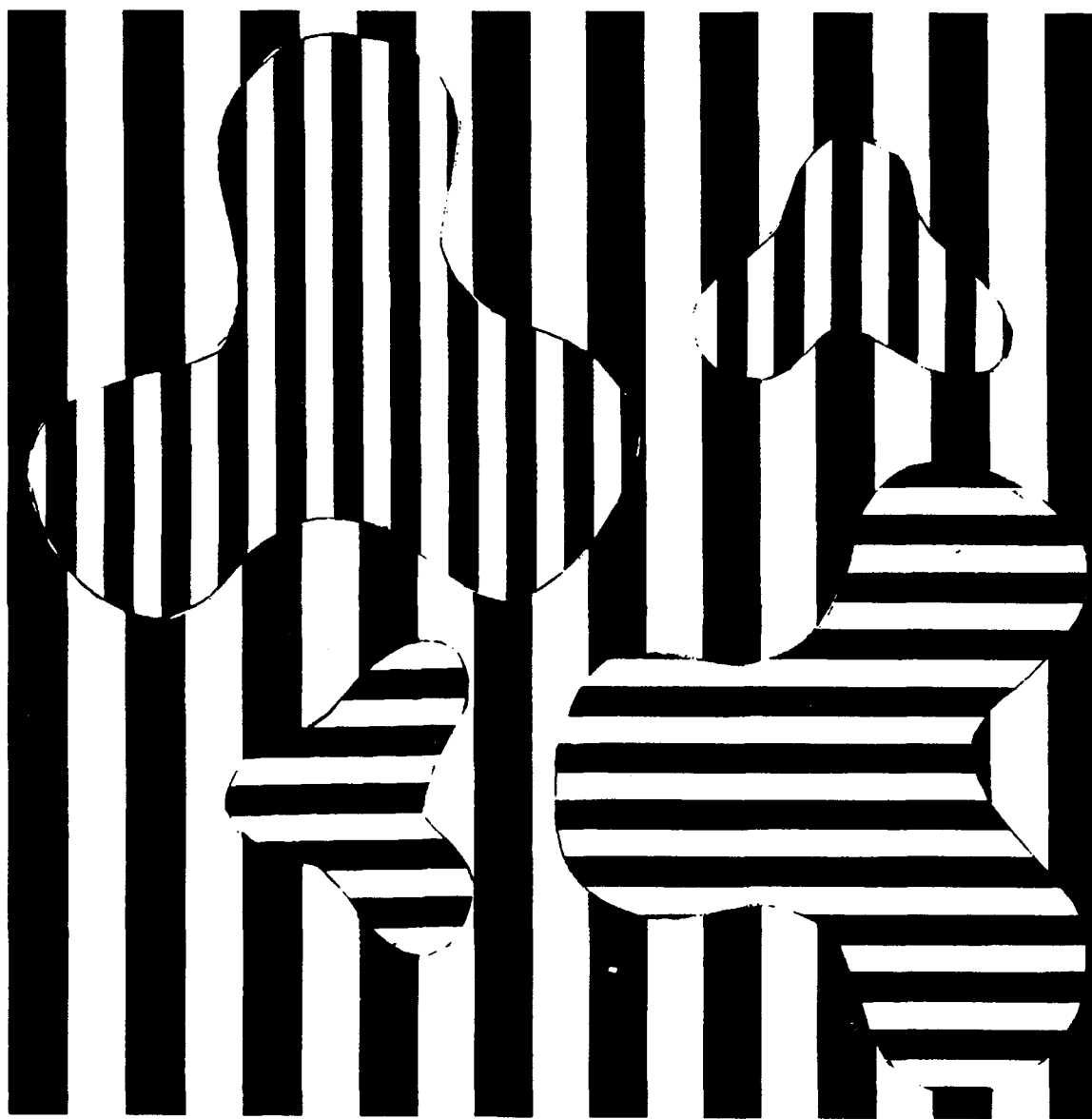


Figure D.2. Example of a simple texture slide with a 10 cycle background and two 20 cycle textures in parallel and perpendicular orientations

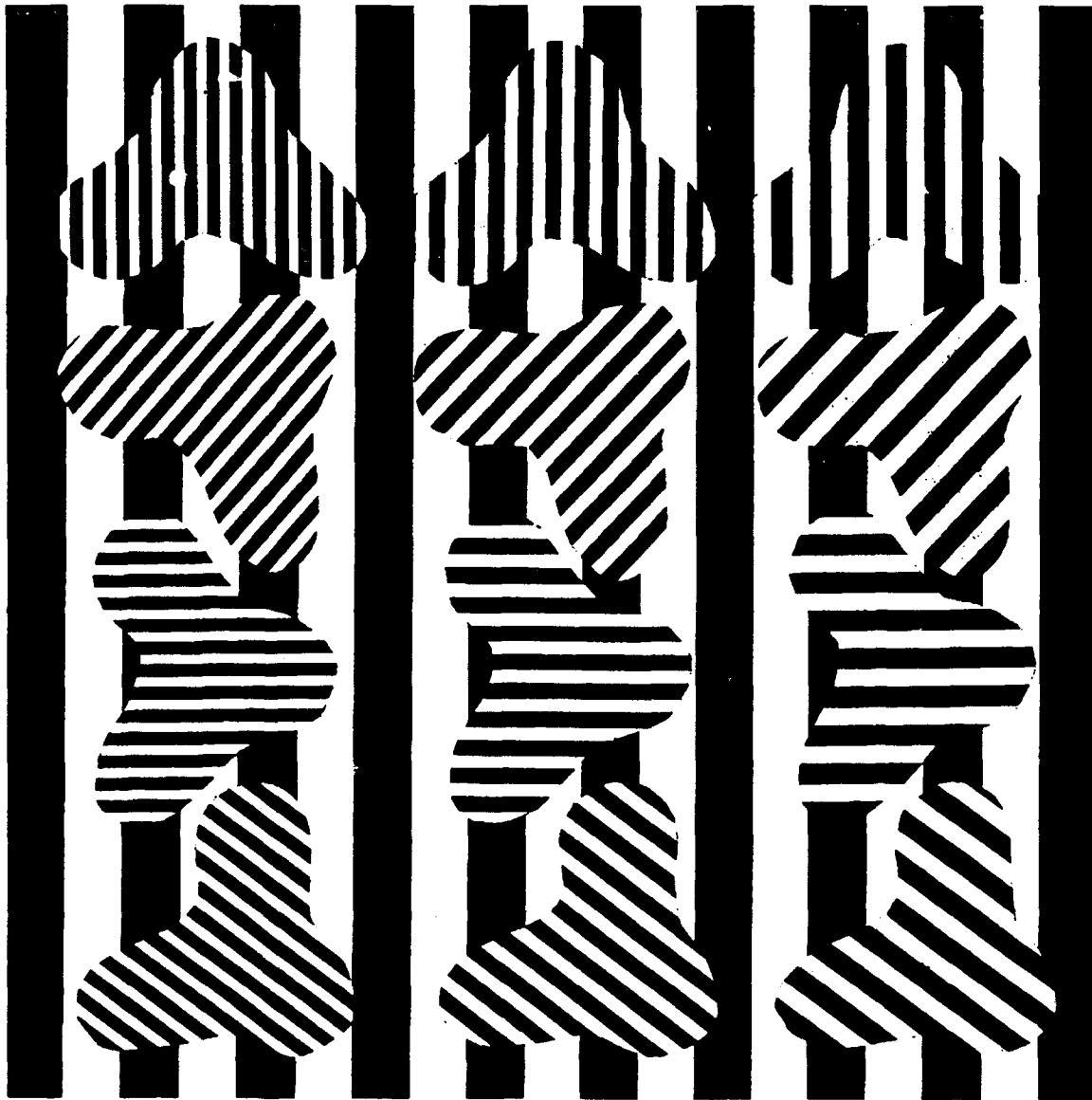


Figure D.3. Example of a more complex simple texture slide with a 10 cycle background and three other textures consisting of 30, 40, and 50 cycles at 0, 45, 90, and 135° orientations

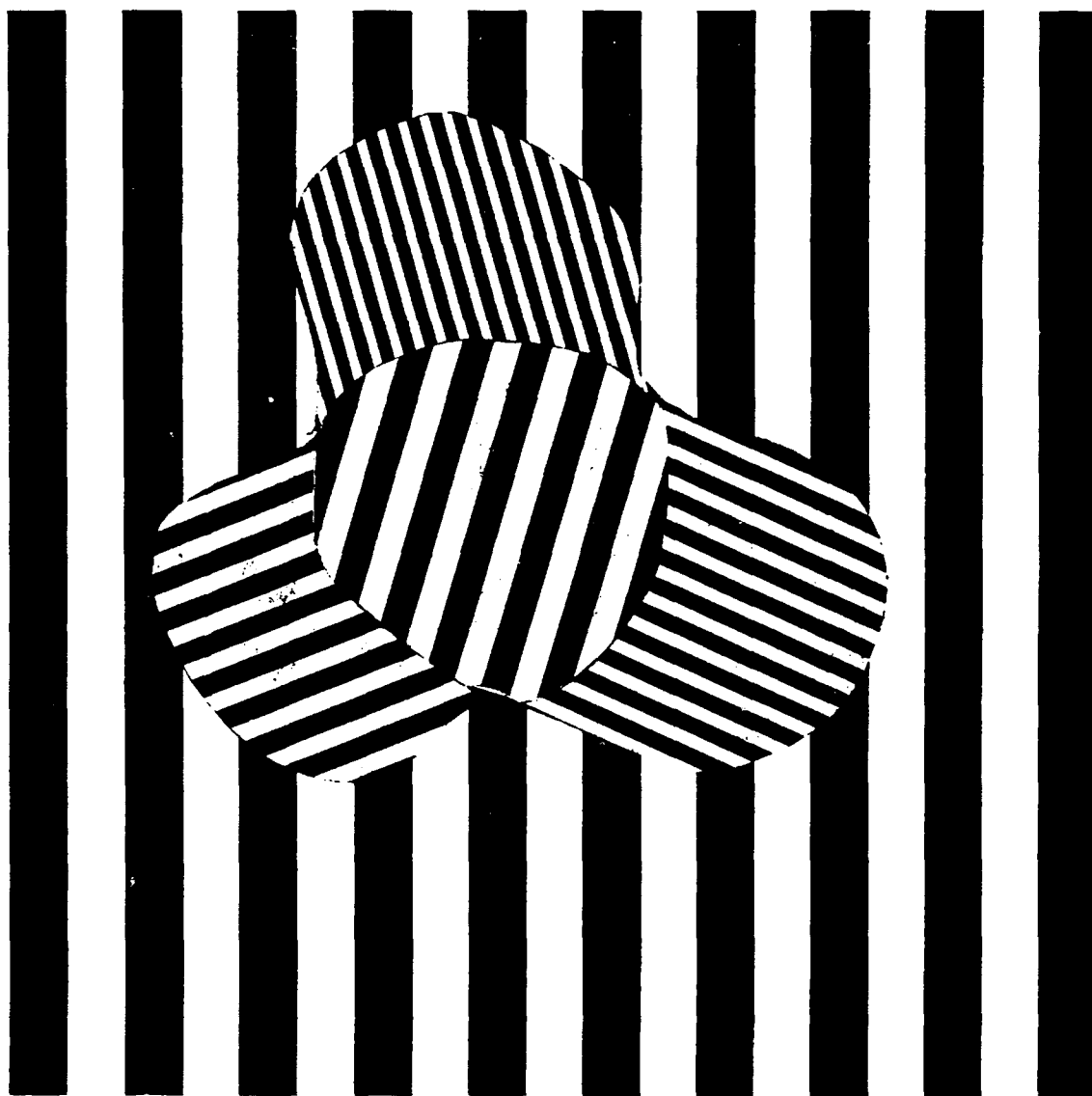


Figure D.4. Example of a more complex simple texture slide with a 10 cycle background and four other textures consisting of a 20 cycle center texture and 30, 40, and 50 cycle outer lobes, all at different orientations

Bibliography

1. AT&T. *Truevision Advanced Raster Graphics Adapter: TARGA 8, M8, 16, 24, and 32, User's Guide*, 1985. Release 1.1.
2. AT&T. *Truevision Advanced Raster Graphics Adapter: TARGA 8, M8, 16, 24, and 32, Software Tools Notebook*, 1986. Release 3.0.
3. Ayer, Captain Kevin W. *Gabor Transforms for Forward Looking InfraRed Image Segmentation*. MS thesis, AFIT/GE/ENG/89D-1, School of Engineering, Air Force Institute of Technology (AU), Wright-Patterson AFB OH, December 1989 (AD-A215046).
4. Barnes, Thomas H., et al. "Phase-only modulation using a twisted nematic liquid crystal television," *Applied Optics*, 28(22):4845-4852 (November 1989).
5. Bovik, Alan Conrad, et al. "Multichannel Texture Analysis Using Localized Spatial Filters," *IEEE Transactions on Pattern Analysis and Machine Intelligence*, 12(1):55-73 (January 1990).
6. Bush, Captain Larry F. *The Design of an Optimum Alphanumeric Symbol Set for Cockpit Displays*. MS thesis, AFIT/GE/EE/77-11, School of Engineering, Air Force Institute of Technology (AU), Wright-Patterson AFB OH, December 1977 (AD-A053447).
7. Casasent, David, et al. "Real-time deformation invariant optical pattern recognition using coordinate transformations," *Applied Optics*, 26(5):938-942 (March 1987).
8. Cheng, Yih-Shyang and Jiunn-Yann Lin. "Experimental use of a low cost liquid crystal TV in multiplex holography," *Applied Optics*, 28(5):829-830 (March 1989).
9. Childress, Timothy G. and J. Thomas Walrond. *Position, Scale, and Rotation Invariant Optical Pattern Recognition For Target Extraction and Identification*. MS thesis, AFIT/GE/ENG/88D-4, School of Engineering, Air Force Institute of Technology (AU), Wright-Patterson AFB OH, December 1988.
10. Cline, Captain John D. *Hybrid Optical/Digital Architecture for Distortion Invariant Pattern Recognition*. MS thesis, AFIT/GEO/ENG/89D-02, School of Engineering, Air Force Institute of Technology (AU), Wright-Patterson AFB OH, December 1989 (AD-867524).
11. Daugman, John G. "Complete Discrete 2-D Gabor Transforms by Neural Networks for Image Analysis and Compression," *IEEE Transactions on Acoustics, Speech, and Signal Processing*, 36(7):1169-1179 (July 1988).
12. Gaskill, J. D. *Linear Systems, Fourier Transforms, and Optics*. New York: John Wiley & Sons, 1978.
13. Goodman, J. W. *Introduction to Fourier Optics*. New York: McGraw-Hill Book Company, 1968.
14. Gregory, Don A. "Real-time pattern recognition using a modified liquid crystal television in a coherent optical correlator," *Applied Optics*, 25(4):467-469 (February 1986).

15. Hamadani, Naser A. *Automatic Target Cueing in IR Imagery*. MS thesis, School of Engineering, Air Force Institute of Technology (AU), Wright-Patterson AFB OH, December 1981 (AD-A115480).
16. Horev, Moshe. *Picture Correlation Model for Automatic Machine Recognition*. MS thesis, School of Engineering, Air Force Institute of Technology (AU), Wright-Patterson AFB OH, December 1980.
17. Hudson, Tracy D., et al. "Real time optical correlator architectures using a deformable mirror spatial light modulator," *Applied Optics*, 28(22):4853-4860 (November 1989).
18. Hughes, Kenneth D. *Suitability and Applications of Liquid Crystal Televisions In Optical Pre-processors*. MS thesis, AFIT/GE/ENG/86D-6, School of Engineering, Air Force Institute of Technology (AU), Wright-Patterson AFB OH, December 1986 (AD-A177603).
19. Hughes, Kenneth D., et al. "Optical preprocessing using liquid crystal televisions," *Applied Optics*, 26(6):1042-1044 (March 1987).
20. Jutamulia, S., et al. "Real-time noncoherent correlator using liquid crystal television," *Optical Communications*, 64(2):115-119 (October 1987).
21. Lee, Wai-Hon. "Computer-Generated Holograms: Techniques and Applications." In Wolf, E., editor, *Progress in Optics XVI*, chapter III, New York: North-Holland Publishing Company, 1978.
22. Li, Yao, et al. "Liquid crystal TV-based white light optical tracking novelty filter," *Applied Optics*, 28(22):4861-4864 (November 1989).
23. Liu, Hua-Kuang and Tien-Hsin Chao. "Liquid crystal television spatial light modulators," *Applied Optics*, 28(22):4772-4780 (November 1989).
24. Liu, Hua-Kuang, et al. "Optical-data-processing properties of a liquid-crystal television spatial light modulator," *Optics Letters*, 10(12):635-637 (December 1985).
25. Lu, Kanghua and Bahaa E. A. Saleh. "Theory and design of the liquid crystal TV as an optical spatial light modulator," *Optical Engineering*, 29(3):240-246 (March 1990).
26. Mills, Lt Col James P. Personal interview. AFIT, WPAFB OH, 20 May 1990.
27. Mok, Fai, et al. "Real-time computer-generated hologram by means of liquid-crystal television spatial light modulator," *Optics Letters*, 11(11):748-750 (November 1986).
28. Mueller, Captain Michael R. *Investigation of Gabor Filters for Use in Reverse Engineering VLSI Circuits*. MS thesis, AFIT/GE/ENG/89D-35, School of Engineering, Air Force Institute of Technology (AU), Wright-Patterson AFB OH, December 1989 (AD-B138982L).
29. Perez, O. and M. A. Karim. "An efficient implementation of joint Fourier transform correlation using a modified LCTV," *Microwave and Optical Technology Letters*, 2(6):193-196 (June 1989).
30. Perez, Osvaldo. Personal interview., ASD/ENAML, WPAFB, OH, 8 August 1990.
31. Roberts, Richard E., et al. "Three Dimensional Scene Analysis Using Stereo Based Imaging." In *Proceedings of the SPIE Sixth Annual Conference on Applications of Artificial Intelligence, Volume 937*, pages 280-286, Bellingham, WA: SPIE Press, 1988.

32. Robinson, Capt Vicky L. *Hybrid Calculation of Invariant Moments*. MS thesis, AFIT/GEO/ENG/88D-3, School of Engineering, Air Force Institute of Technology (AU), Wright-Patterson AFB OH, December 1988 (AD-A158802).
33. Roggemann, Captain Michael C. *Multiple Sensor Fusion for Detecting Targets in FLIR and Range Images*. PhD dissertation, School of Engineering, Air Force Institute of Technology (AU), Wright-Patterson AFB OH, June 1989 (AD-A207577).
34. Ruck, Captain Dennis W., et al. "Multisensor Target Detection and Classification." In *Proceedings of the SPIE Conference on Infrared Sensors and Sensor Fusion, Volume 931*, pages 14-21, Bellingham, WA: SPIE Press, 1988.
35. Sharp - Electronics Components Group. *Device Specification For TFT-LCD Module - Model No. LQ424A01 (TENTATIVE)*, September 1989.
36. Tam, Eddy C., et al. "Autonomous real-time object tracking with an adaptive joint transform correlator," *Optical Engineering*, 29(4):314-320 (April 1990).
37. Tong, Captain Carl Tong, et al. "Multisensor Data Fusion of Laser and Forward Looking Infrared (FLIR) for Target Segmentation and Enhancement." In *Proceedings of the SPIE Conference on Infrared Sensors and Sensor Fusion, Volume 782*, pages 10-19, Bellingham, WA: SPIE Press, 1987.
38. Turner, M. R. "Texture Discrimination by Gabor Functions," *Biological Cybernetics*, 55:71-82 (1986).
39. Yu, Francis T. S., et al. "Adaptive real-time pattern recognition using a liquid crystal TV based joint transform correlator," *Applied Optics*, 26(8):1370-1372 (April 1987).
40. Yu, Francis T. S., et al. "Multiple channel optical correlator via rotating grating on LCTV," *Applied Optics*, 27(18):3770-3772 (September 1988).

Vita

Captain Christopher P. Veronin [REDACTED] He graduated from Sahuaro High School in Tucson, Arizona in 1978 and attended Arizona State University (ASU) in Tempe, Arizona where he received the degree of Bachelor of Science in Electrical Engineering in May 1984. During his last year at ASU, he was accepted into the College Senior Engineering Program of the United States Air Force and upon graduation received his commission from Officer Training School in August 1984. His first assignment was to the Foreign Technology Division at Wright-Patterson AFB, OH, where he served as a Foreign Telecommunications Analyst, Command, Control, and Communications Division until entering the School of Engineering, Air Force Institute of Technology in May 1989.

[REDACTED]

